

Fractional Chern Insulators Transition in Non-ideal Flat Bands of Twisted Mono-bilayer Graphene

Moru Song^{1,2,3} and Kai Chang^{2,*}

¹*State Key Laboratory of Semiconductor Physics and Chip Technologies,
Institute of Semiconductors, Chinese Academy of Sciences, Beijing 100083, China*

²*Center for Quantum Matter, Zhejiang University, Hangzhou 310027, China*

³*College of Materials Science and Opto-electronic Technology,
University of Chinese Academy of Sciences, Beijing 100049, China*

(Dated: November 25, 2025)

Fractional Chern insulators (FCIs) in ideal flat bands with Chern number C are commonly understood as color-entangled states constructed from C copies of the lowest Landau level. In realistic moiré systems, however, the band geometry is generally non-ideal, and the mechanism that stabilizes such FCIs remains unclear. Using twisted monolayer–bilayer graphene as a platform, we find two FCIs separated by a continuous transition driven by a geometric instability of the Bloch wave functions. Below the transition, the target $C = 2$ conduction band is geometrically stable, and the resulting fractional phase is naturally described by the Halperin-(112) state. Above the transition, the system is geometrically unstable, entering a Laughlin-1/3 phase that persists despite further degradation of standard quantum-geometry indicators. To account for this unconventional phenomenon, we propose a color-separation mechanism beyond global geometric indicators: in the geometrically unstable regime, interactions hybridize electronic states near the K point and generate an emergent ideal color component that supports the FCI. We corroborate this picture by applying a weak perpendicular magnetic field that acts as a “color separator,” directly visualizing the ideal subcomponent in the single-particle level. Together, these results establish mechanisms which non-ideal flat bands stabilize FCIs, substantially enlarging their viable parameter space and clarifying the role of quantum geometry in strongly correlated topological phases.

Introduction.—Fractional Chern insulators (FCIs) serve as lattice analogs of fractional quantum Hall (FQH) states and have been experimentally observed in flat bands with $|C| = 1$ [1–6]. Unlike conventional FQH phases in partially filled Landau levels, FCIs can also arise in nearly flat bands with higher Chern numbers $|C| > 1$ [7–10], where the ground states often resemble multicomponent Halperin wavefunctions [8, 10–14] obtained by decomposing the original band into C effective lowest Landau levels (LLs) or “colors” [15–17]. This mapping is exact under the ideal flat-band (quantum-geometric trace) condition, which confines vortices bound to electrons within the band subspace and yields purely holomorphic Bloch functions—mirroring the anticlockwise LLL orbitals—so that FCI stability can be predicted from single-particle quantum geometry alone [18, 19]. In realistic non-ideal bands beyond LLL, however, vortex attachment becomes nontrivial, Bloch functions acquire anti-holomorphic parts [18–20], and the simple color-layer mapping may fail—making explicit many-body calculations essential, as universal single-particle stability criteria remain unknown. Yet, which FCIs survive, and the reason why they can be stabilized in such non-ideal flat bands with $|C| \neq 1$ is still unknown.

In this Letter, we demonstrate and explain a topological transition between two distinct fractional Chern insulators realized in a non-ideal flat band, and show that it is driven by a geometric instability of the Bloch wave functions. Using twisted monolayer–bilayer graphene (tMBG) as a platform, we analyze the $C = 2$ conduction

flat bands of the continuum model (CM) under a perpendicular electric field [21–23] and first benchmark them within the Hartree–Fock (HF) approximation. As the CM parameter κ is tuned, the single-particle quantum geometry degrades, and an interaction-induced Chern number transition happens at large κ . More specifically, exact diagonalization (ED) results show two distinct FCI phases separated by a continuous transition at $\kappa_c = 0.55$. Interestingly, this transition is driven by an intrinsic geometric instability of the Bloch states revealed by our hybrid-Wannier analysis at both non-interacting and HF level. For $\kappa < \kappa_c$, the target $|C| = 2$ conduction band is geometrically stable and effectively decomposes into two independent $C = 1$ even-odd sectors similar to ideal cases. After that, interactions then stabilize a Halperin-(112)–like phase with non-chiral edge modes [24]. For $\kappa > \kappa_c$, the wavefunction become geometric unstable, and the system enters a Laughlin-type FCI with an enhanced derivation from the ideal limit. To account for such unconventional phenomenon, we propose a “color-separation” conjecture: a non-ideal flat band can be regarded as a superposition of a partially ideal Chern component and additional non-ideal components. After that, interactions locally hybridize original colors when the wave function is geometric unstable, leaving one ideal component to support the FCI ground states. Finally, by introducing a weak perpendicular magnetic field [4, 22, 25–27] as a “color separator,” we extract the band components and identify perfectly ideal subcomponents at $\kappa > \kappa_c$ that support the FCI, thereby substantiating

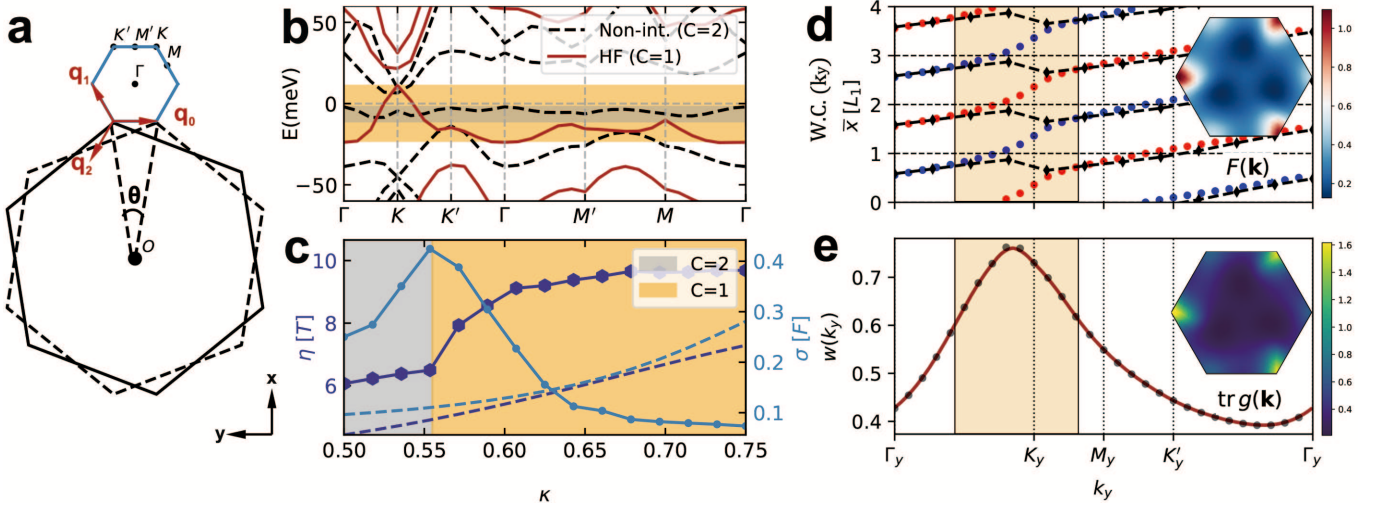


FIG. 1. (a) Moiré Brillouin zone of tMBG. (b) Non-interacting bands (dashed) and HF level bands of $\xi = 1, s = \uparrow$ based on CM model at $\kappa = 0.62$, with target conduction bands shaded in gray and orange. (c) Variation of geometric criteria in terms of κ for non-interacting (dashed) and HF cases (dotted). Different Chern number for HF results in certain region is shaded in colors. (d) Evolution of Wannier centers as a function of k_y for noninteracting (dotted) and HF (dashed black) cases. Blue and red dots denote the even and odd sectors, respectively [17]. The y -axis spans four unit cells; L_1 denotes the length of the moiré unit-cell vector. Insert: berry curvature distribution of non-interacting case. (e) The spread of hwF $w(k_y)$ evolution with k_y of $C = 2$ non-interacted band. The shaded box represents region where the berry curvature concentrate. Insert: Metric trace distribution of non-interacting case.

the conjecture. Importantly, such mechanism for stabilizing FCIs in non-ideal flat bands appear generic: they extend naturally to higher-Chern bands, broadening the known conditions under which FCIs can emerge.

Quantum geometry indicators.—For generic (non-ideal) flat bands, departures from the ideal LLL geometry can be captured by two geometric measures [4, 18]: the trace-condition violation $\eta(\mathbf{k}) = \text{Tr } g(\mathbf{k}) - |F(\mathbf{k})|$ and the uniformity of Berry curvature quantified by its standard deviation $\sigma[F(\mathbf{k})]$. Here $g_{\mu\nu}(\mathbf{k}) = \text{Re } T_{\mu\nu}$ is the quantum metric and $F(\mathbf{k}) = -2 \text{Im } T_{xy}$ the Berry curvature, with $T_{\mu\nu} = \langle \partial_{k^\mu} u_{\mathbf{k}} | (1 - |u_{\mathbf{k}}\rangle\langle u_{\mathbf{k}}|) | \partial_{k^\nu} u_{\mathbf{k}} \rangle$ the quantum geometric tensor. These quantities diagnose how closely a band mimics $|C|$ decoupled copies of the LLL.

Continuum model of tMBG.—As illustrate in Fig. 1 (a), tMBG consists of a monolayer stacked atop a Bernal bilayer with a small twist angle θ , giving rise to a moiré superlattice and mini Brillouin zone. The CM model of tMBG gives [21–23],

$$H_0(\mathbf{k}) = \begin{bmatrix} h_\theta(\mathbf{k}) & T^\dagger(\mathbf{r}) & 0 \\ T(\mathbf{r}) & h_\theta(\mathbf{k}) & W^\dagger(\mathbf{k}) \\ 0 & W(\mathbf{k}) & h_\theta(\mathbf{k}) \end{bmatrix}, \quad (1)$$

where \mathbf{k} is limited in the first Brillouin zone (1BZ), $h_\theta(\mathbf{k}) = -\hbar v_0 \xi (\sigma_x k_1 + \sigma_y k_2)$ is the Dirac Hamiltonian with $(k_1, k_2) = (k_x - K_x^\xi, k_y - K_y^\xi) R^T(\theta)$, $\xi = \pm 1$ the valley index, and $R(\theta)$ the rotation matrix. The standard Slonczewski-Weiss-McClure form [28] of AB-stacked interlayer coupling is $W(\mathbf{k}) = \begin{bmatrix} \hbar v_4 k_+ & \gamma_1 \\ \hbar v_3 k_- & \hbar v_4 k_+ \end{bmatrix}$, with

$k_\pm = \xi k_1 \pm i k_2$ and $\hbar v_\mu = \frac{\sqrt{3}a}{2} \gamma_\mu$. The lattice constant is $a = 2.46$, and hopping parameters are $\gamma_0 = -2.61$ eV and $\gamma_1 = 0.361$ eV. In contrast to chiral twisted multi-layer graphene model [8, 18], where $\gamma_3 = \gamma_4 = 0$, here we have realistic $\gamma_3 = 0.283$ eV, $\gamma_4 = 0.140$ eV [23].

The moiré interlayer tunneling $T(\mathbf{r}) = \sum_{s=0}^2 \mathcal{T}_s e^{i\mathbf{q}_s \cdot \mathbf{r}}$ is encoded with lowest harmonica components $\mathcal{T}_s = w_{AA} \sigma_0 + w_{AB} [\cos(s\xi\varphi) \sigma_x + \sin(s\xi\varphi) \sigma_y]$, where $\varphi = 2\pi/3$, $\xi = \pm 1$ is the valley index, and $s = 0, 1, 2$ labels the three C_3 -related momentum transfers $\mathbf{q}_s = R^s(\varphi) \cdot \mathbf{q}_0$ with $\mathbf{q}_0 = \frac{8\pi}{3a} \sin(\theta/2) [0, -1]^T$. The tunneling strength ratio is defined as $\kappa = w_{AA}/w_{AB}$ accounting for the lattice relaxation effect, which usually regard as an experimental parameter that positive related to $\eta[T]$. Furthermore, the external bias $V_{\text{pot}} = 50$ meV and a sublattice-staggered potential $M = 30$ meV, simulating substrate effects within the zeroth layer, are added independently.

Band structure signature.—As a initial test of interaction effect, we begin by performing non-interacting and HF calculation at integer filling $\nu = 1$ of $C = 2$ conduction band (See End Matter for projected interaction Hamiltonian). The resulting non-interacting band structure at $\kappa = 0.62$ is shown in Fig. 1(b), exhibiting a narrow bandwidth of approximately 9 meV and a total Chern number $C = 2$ [22], with both berry curvature and metric trace concentrate near K points [Insert of Fig. 1(d, e)]. However, upon introducing interactions, the target flat band's bandwidth increases significantly to 32 meV (see End Matter for explanation), and the Chern number spontaneously reduces to $C = 1$. Inter-

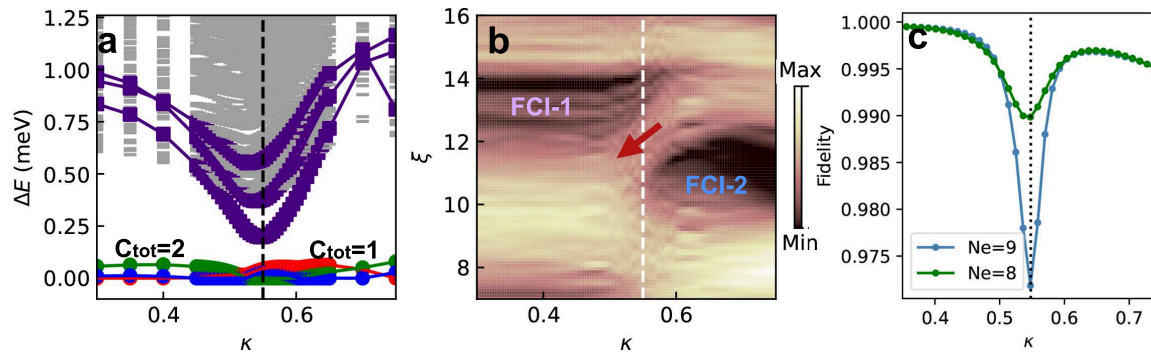


FIG. 2. ED calculation on $N_{orb} = 4 \times 6$ momentum mesh with $N_e = 8$ electrons. FCI-1 and FCI-2 stand for FCIs with $C = 2/3$ and $C = 1/3$. (a) Variation of ED energy levels with κ , where ΔE measures relative ground states. Degenerated 3-fold ground states are labeled with red, green and blue. The lowest 3-excited states with same total momentum with respect to ground states are labeled in purple. (b) Variation of PES density of states with κ , where $e^{-\xi/2}$ is eigenvalue of reduced density matrix ρ_A , which is obtained by bipartiting system into $N_A = 3, N_B = 5$ electrons, 1520 states below FCI-1 gap while 1088 sates below FCI-2 gap (see [29] for details). (c) Density matrix fidelity of ground states for 8 and 9 electrons [29].

estingly, this topological transition is controlled by the interlayer tunneling parameter κ without any band mixing at the critical point, and the Berry curvature near the K points reverses sign discontinuously immediately after the transition, indicating only closing of many body gap [29, 30]. As shown in Fig. 1(c), we compare the evolution of the trace deviation $\eta[T]$ and Berry curvature fluctuation $\sigma[F(\mathbf{k})]$ as functions of κ . In the non-interacting case, both η and σ increase monotonically with κ , indicating a steady departure from the ideal flat band condition. In contrast, when interactions are included, σ exhibits a pronounced peak at $\kappa_c = 0.55$, accompanied by a discontinuous jump in η . Numerical calculations confirm that $\kappa_c = 0.55$ corresponds precisely to the phase boundary between the $|C| = 2$ and $|C| = 1$ regimes. These signatures indicates interaction make bands more close to the general landau levels at $\kappa > \kappa_c$ due to decreasing $\sigma[F]$ after the phase transition, however, more departure from LLL due to increased $\eta[T]$. Although the changing in Chern number is consistent with the FCI transition shown below, our result contrasts with theoretical predictions for FCIs stabilized in rhombohedral multilayer graphene via pre-Hartree-Fock optimization of the single-particle basis [6, 31–33]. In our case, quantum-geometric indicators evaluated after HF, especially the trace condition—do not account for the stabilization of the FCIs.

Geometric instability.— To move beyond global geometric indicators and expose where and how the Bloch wave functions reconstruct across the transition, we analyze the bands in the hybrid-Wannier-function (hWF) representation, which keeps one crystallographic direction (here y) in momentum space while Wannier-localizing the orthogonal direction x , thereby providing a quasi-local probe of single-particle wave-function geometry [17, 29, 34, 35]. In this mixed basis, the Wannier center $\bar{x}(k_y)$ traces a flow whose winding counts the

Chern number, while its spread $w(k_y)$ measures the hWF width and is directly related to the quantum metric (see End Matter and Supplementary Material [29]). Thus the hWF representation offers a spatially resolved link between topology—via the center’s winding—and geometry—via the shape and thickness of the flow.

Figure 1(d) shows the center flow for the noninteracting $C = 2$ band (dotted), resolved into even and odd sectors [17]. Near $k_y = K_y$, the two branches bend toward each other, precisely where Fig. 1(c) indicates enhanced Berry-curvature inhomogeneity. Consistently, Fig. 1(e) reveals a marked increase of $w(k_y)$ in the same window, reflecting an amplified spreads of hWF. Curvature concentration draws the trajectories together in momentum space, while metric enhancement broadens the hWFs in real space and increases their mutual overlap.

Including interactions, the HF result shown as a dashed black curve in Fig. 1(d) magnifies this geometrically seeded tendency: nearby branches merge and reconnect within the K_y neighborhood, changing the net winding from two to one and realizing the $C = 2 \rightarrow 1$ jump. At the critical point $\kappa_c = 0.55$, the center flow develops a momentum-space ambiguity: integrating from $k_y = 0$ upward yields $C = 2$, whereas integrating downward yields $C = 1$, signaling imminent reconnection. Taken together, these observations define the *instability* of Bloch wave functions: a local combination of curvature focusing and metric amplification that induces in the center flow a strong tendency to reconnect, so that even weak inter- \mathbf{k} perturbations can change its winding and hence the Chern number.

Topological Transition of FCIs.— Since interactions can induce a Chern-number transition at integer filling in a full-band calculation, it is natural to extend a similar analysis to fractional fillings within a single-band projection without band mixing. As shown in Fig. 2(a), the neutral excitation mode softens in the

same total-momentum sector as κ approaches 0.55, indicating a phase transition consistent with the HF prediction [36]. This transition is further corroborated by the particle entanglement spectrum (PES) [37–39] and the many-body Chern number (MBC). In Fig. 2(b), the PES exhibits a clear gap whose level counting below the gap follows the (k, r) admissible rule [39], meaning that there are at most k particles in any set of r consecutive orbitals. For $k = 1$, the counting is given by $D_{(1,r)}(N_{\text{orb}}, N_e) = N_{\text{orb}} C_{N_{\text{orb}} - (r-1)N_e - 1}^{N_e - 1} / N_e$, where $N_{\text{orb}} = N_x \times N_y$ [40]. In addition, the MBC is obtained by inserting flux through twisted boundary conditions [29]. Finally, as shown in Fig. 2(c), the fidelity of the degenerate ground states displays a pronounced dip near the critical point, signaling a continuous phase transition between two FCIs [41].

For $\kappa < 0.55$, we find a threefold degenerate ground-state manifold, which we identify as a Halperin-(112) phase (FCI-1). Each ground state carries Chern number $C = 2/3$, and the particle entanglement spectrum (PES) exhibits a clear gap with $D_{(1,2)}(24, 3) = 1520$ levels below it, consistent with the (1, 2) admissible rule. Conventional FCIs realized in higher-Chern-number bands at fillings $\nu = p/(2p|C| + 1)$ ($p, |C| \in \mathbb{Z}^+$) are ruled out by their distinct ground-state degeneracy, PES counting [40, 42, 43], Hall conductance, and fillings [3, 10, 29]. As shown in the End Matter, the Coulomb ground state of model Halperin-(112) states [44–46] exhibits the same PES counting as obtained here.

We rationalize the stability of the Halperin-(112) phase in a non-ideal flat band from two complementary viewpoints. First, “non-ideal” band geometry—e.g., nonuniform Berry curvature and violations of the trace condition—precludes the existence of a globally holomorphic Bloch-frame [10]. Second, in the composite-fermion (or parton) description, the Halperin (112) state at $\nu = 2/3$ belongs to the “negative” Jain sequence $\nu = p/(2p|C| - 1)$. One binds two flux quanta parallel to the external magnetic field to each electron ($2p = 2$), so that the composite fermions experience an effective magnetic field B^* opposite in sign to the physical field and form a spin-singlet integer quantum Hall state with two filled composite-fermion Λ -levels; one then typically applies the LLL projection \mathcal{P}_{LLL} (see End Matter) to restore holomorphicity, a step that does not, in the continuum, alter the K -matrix data and hence does not change the type of topological order [47, 48]. Taken together, although the deviation from the LLL ideal injects anti-holomorphic weight into the Chern-band representation, for nonchiral topological orders such as Halperin-(112), characterized by $\det K < 0$, this non-holomorphicity is less detrimental than it is for the usual fully chiral Jain sequence with positive-definite K . Consequently, the (112) phase can remain comparatively robust in non-ideal flat bands.

As $\kappa > 0.55$, the identification of the ground state

is straightforward. The PES exhibits a sharp gap with $D_{(1,3)}(24, 3) = 1088$ states below it, matching the (1, 3) admissible rule that characterizes the $\nu = 1/3$ Laughlin-like FCI (FCI-2). Concurrently, the many-body Chern number for each of the nearly threefold degenerate ground states is $C = 1/3$, confirming this interpretation [29]. However, the stabilization of Laughlin-like FCI in non-ideal flat bands is very different from Halperin-(112) states for its should supported by holomorphic wave functions. To explain the origin of such stabilization mechanism, we propose the following conjecture.

Color separation conjecture.— Motivated by color decompositions in ideal flat bands [8–10] and by the composite-fermion (CF) picture of the FQH effect [47, 48], we posit that a generic non-ideal flat band admits the decomposition

$$u_{\mathbf{k}}(\mathbf{r}) = \sum_{\beta} D_{\mathbf{k}\beta}(\mathbf{r}) v_{\mathbf{k}}^{\beta}(\mathbf{r}), \quad (2)$$

where $v_{\mathbf{k}}^{\beta}$ are Landau-level-like “color” components, analogous to the Λ -levels in the CF construction. Each component is adiabatically connected to an exact LL sector and carries a Chern number $C_{\beta} = \pm 1$, with the total Chern number satisfying $C = \sum_{\beta} C_{\beta}$. Additionally, $D_{\mathbf{k}\beta}(\mathbf{r})$ is connected to the real space distribution of charge. To quantify how “LLL-like” each sector is, we define component-resolved deviations η^{β} as non-ideal generalizations of η . On the one hand, some $v_{\mathbf{k}}^{\beta}$ may be higher-LL-like [19] and nonchiral, potentially supporting unconventional FCI states. On the other hand, sectors with smaller η^{β} are energetically preferred in the ground state under interactions [49], leading to selective occupation/hybridization of the most ideal components—an effect we term *color separation*. Specifically, in our case, when $\kappa < \kappa_c$, in the hybrid-Wannier picture the even/odd branches remain well separated and the Wannier-function spread is modest; we can therefore regard the $C = 2$ band as two $C = 1$ even/odd branches without invoking interaction-induced wave-function instability [17]. However, when $\kappa > \kappa_c$, interactions recombine the even and odd branches, potentially modifying the color-separation outcome—for example, by selecting an ideal $C = 1$ component that supports the formation of a Laughlin-like FCI. The decomposition in Eq. (2) is generally nonunique, and the realized separation pattern can depend on interaction details when the wave function is near an instability. Crucially, even when the overall band is nonideal, a Laughlin-like FCI can still be stabilized provided that at least one color sector remains close to the ideal limit.

Color separation under magnetic field.—When $\kappa > \kappa_c$, as argued above, the Bloch wave functions develop an instability near the K point. This instability is intrinsic to the band’s quantum geometry: it need not be driven solely by interactions—any perturbation that couples different momenta can activate it. Motivated by this, we

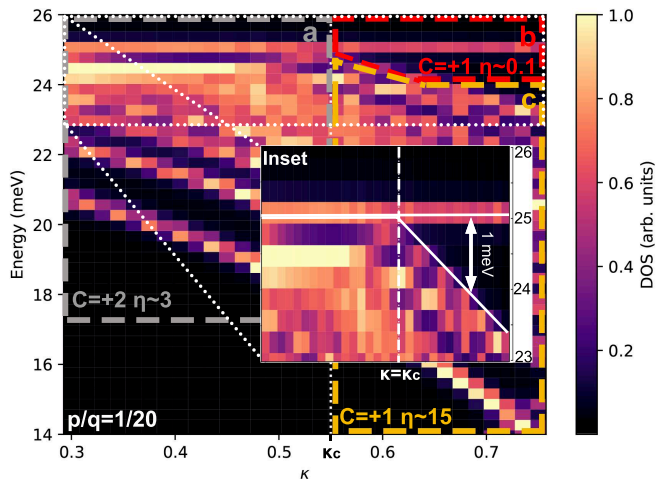


FIG. 3. Density of states (DOS) of the target flat bands versus κ under a weak magnetic field with $p/q = 1/20$. In region **a**, the bands are nearly ideal and, for $\kappa > \kappa_c = 0.55$, split into two branches. Region **b** hosts an exactly ideal flat band, whereas region **c** is non-ideal and offset from **b** by ~ 1 meV. Inset: magnified view of 23–26 meV, with white lines are guided for eyes.

apply a weak perpendicular magnetic field with rational flux $\phi/\phi_0 = p/q = 1/20$ per moiré unit cell to peel out the ideal color component already at the single-particle level. As shown in Fig. 3, we track the target conduction band as a function of κ . Strikingly, in line with the FCI and HF phenomenology, a pronounced spectral splitting appears in the vicinity of the same critical point $\kappa = \kappa_c$. For $\kappa < \kappa_c$ [region **a** in Fig. 3], the weak field preserves a $C = +2$ band that remains non-ideal with $\eta \sim 3$. For $\kappa > \kappa_c$, a clear splitting develops: around 23–25 meV, a gap of order 1 meV opens and an isolated, nearly ideal $C = 1$ flat band with $\eta \sim 0.1$ detaches, while its split partners become strongly non-ideal with $\eta \sim 15$ [50]. To avoid confusion, we note that although in Fig. 3 the ideal component appears at a relatively higher single-particle energy, this is not inconsistent with its dominant contribution to the many-body ground state: once interactions are included, the ideal component typically gains more Fock energy and is therefore preferentially pulled down to form the ground state [51]. These observations provide single-particle evidence for our color-separation conjecture. In summary, for bands with intrinsic geometric instability, the ideal color component can be extracted by perturbations that induce inter- \mathbf{k} scattering (e.g., interactions or a weak magnetic field), thereby separating it from the non-ideal sectors. This ultimately explains the stability of Laughlin-like FCI-2.

Additionally, we also calculated trace condition for stronger fields as depicted in Fig. 6 (see End Matter). Note that magnetic subbands with different Chern number and trace condition under stronger field may not count for the color separation. Halperin-(332) states may

be stabilized in $C = 2$ bands under strong negative field for decreased η shown in Fig. 6(a, c, green line). Spectral signatures of FCI at $n/3$ and $n/5$ filling are recently observed in experiment for $C = 2$ conduction bands under finite magnetic field of tMBG [52], consisting with our results.

Conclusion.—We identify a geometric instability and color separation mechanism that govern FCI transitions in non-ideal flat bands with $|C| > 1$. Using HF and ED, we show that interaction-driven reorganization of the band’s quantum geometry spontaneously lowers the Chern number from $|C| = 2$ to $|C| = 1$ at $\kappa = \kappa_c$, producing a continuum phase transition between distinct FCI phases. For geometric stable cases, non-ideal flat bands can host FCIs with *non-chiral* edge states, exemplified by Halperin ($m m n$) states with $m < n$. For geometric unstable cases, a non-ideal band may contain an ideal color sector, interactions (or other inter- \mathbf{k} scattering perturbations) perform color separation that isolates this sector and stabilizes a FCI with *chiral* edge states—accounting for the observed robustness of the Laughlin-like phase. These results position tMBG as a controlled platform to probe interaction–geometry interplay and to engineer topological phase transitions in moiré systems.

Note added.—During the preparation of this work, we are aware of the phase transition between Halperin and abnormal Laughlin states is also found in twisted double bilayer graphene [53].

We acknowledge Zhao Liu for helpful discussion. This work is supported by the National Natural Science Foundation of China (No. 12488101) and the Innovation Program for Quantum Science and Technology (Grant No. 2024ZD0300104).

* kchang@zju.edu.cn

- [1] N. Regnault and B. A. Bernevig, Fractional chern insulator, *Phys. Rev. X* **1**, 021014 (2011).
- [2] B. A. Bernevig and N. Regnault, Emergent many-body translational symmetries of abelian and non-abelian fractionally filled topological insulators, *Phys. Rev. B* **85**, 075128 (2012).
- [3] Z. Liu and E. J. Bergholtz, Recent developments in fractional chern insulators, in *Encyclopedia of Condensed Matter Physics* (Elsevier, 2024) p. 515–538.
- [4] Y. L. Xie, A. T. Pierce, J. M. Park, D. E. Parker, E. Khalaf, P. Ledwith, Y. Cao, S. H. Lee, S. W. Chen, P. R. Forrester, K. Watanabe, T. Taniguchi, A. Vishwanath, P. Jarillo-Herrero, and A. Yacoby, Fractional chern insulators in magic-angle twisted bilayer graphene, *Nature* **600**, 439 (2021).
- [5] J. Cai, E. Anderson, C. Wang, X. Zhang, X. Liu, W. Holtzmann, Y. Zhang, F. Fan, T. Taniguchi, K. Watanabe, Y. Ran, T. Cao, L. Fu, D. Xiao, W. Yao, and X. Xu, Signatures of fractional quantum anomalous hall states in twisted mote2, *Nature* **622**, 63 (2023).
- [6] Z. Lu, T. Han, Y. Yao, A. P. Reddy, J. Yang, J. Seo,

- K. Watanabe, T. Taniguchi, L. Fu, and L. Ju, Fractional quantum anomalous hall effect in multilayer graphene, *Nature* **626**, 759 (2024).
- [7] Z. Liu, E. J. Bergholtz, H. Fan, and A. M. Läuchli, Fractional chern insulators in topological flat bands with higher chern number, *Phys. Rev. Lett.* **109**, 186805 (2012).
- [8] J. Wang and Z. Liu, Hierarchy of ideal flatbands in chiral twisted multilayer graphene models, *Phys. Rev. Lett.* **128**, 176403 (2022).
- [9] J. Wang, S. Klevtsov, and Z. Liu, Origin of model fractional chern insulators in all topological ideal flatbands: Explicit color-entangled wave function and exact density algebra, *Phys. Rev. Res.* **5**, 023167 (2023).
- [10] J. Dong, P. J. Ledwith, E. Khalaf, J. Y. Lee, and A. Vishwanath, Many-body ground states from decomposition of ideal higher chern bands: Applications to chirally twisted graphene multilayers, *Phys. Rev. Res.* **5**, 023166 (2023).
- [11] B. I. Halperin, Theory of the quantized hall conductance, *Helv. Phys. Acta* **56**, 75 (1983).
- [12] B. d. z. Jaworowski, N. Regnault, and Z. Liu, Characterization of quasiholes in two-component fractional quantum hall states and fractional chern insulators in $|c|=2$ flat bands, *Phys. Rev. B* **99**, 045136 (2019).
- [13] V. Crépel, N. Claussen, N. Regnault, and B. Estienne, Microscopic study of the halperin–laughlin interface through matrix product states, *Nat. Comm.* **10**, 1860 (2019).
- [14] J.-Z. Ma, R.-Z. Huang, G.-Y. Zhu, J.-Y. Chen, and D.-X. Yao, Fractional chern insulator candidate on a twisted bilayer checkerboard lattice, *Phys. Rev. B* **110**, 165142 (2024).
- [15] G. Tarnopolsky, A. J. Kruchkov, and A. Vishwanath, Origin of magic angles in twisted bilayer graphene, *Phys. Rev. Lett.* **122**, 106405 (2019).
- [16] J. Wang, J. Cano, A. J. Millis, Z. Liu, and B. Yang, Exact landau level description of geometry and interaction in a flatband, *Phys. Rev. Lett.* **127**, 246403 (2021).
- [17] M. Barkeshli and X.-L. Qi, Topological nematic states and non-abelian lattice dislocations, *Phys. Rev. X* **2**, 031013 (2012).
- [18] P. J. Ledwith, A. Vishwanath, and D. E. Parker, Vortexability: A unifying criterion for ideal fractional chern insulators, *Phys. Rev. B* **108**, 205144 (2023).
- [19] M. Fujimoto, D. E. Parker, J. Dong, E. Khalaf, A. Vishwanath, and P. Ledwith, Higher vortexability: Zero-field realization of higher landau levels, *Phys. Rev. Lett.* **134**, 106502 (2025).
- [20] G. Shavit and Y. Oreg, Quantum geometry and stabilization of fractional chern insulators far from the ideal limit, *Phys. Rev. Lett.* **133**, 156504 (2024).
- [21] R. Bistritzer and A. H. MacDonald, Moire bands in twisted double-layer graphene, *Proc. Natl. Acad. Sci. U.S.A.* **108**, 12233 (2011).
- [22] L. Rademaker, I. V. Protopopov, and D. A. Abanin, Topological flat bands and correlated states in twisted monolayer-bilayer graphene, *Phys. Rev. Res.* **2**, 033150 (2020).
- [23] Z. Ma, S. Li, Y.-W. Zheng, M.-M. Xiao, H. Jiang, J.-H. Gao, and X. C. Xie, Topological flat bands in twisted trilayer graphene, *Sci. Bulletin* **66**, 18 (2021).
- [24] X.-G. Wen, *Quantum Field Theory of Many-Body Systems: From the Origin of Sound to an Origin of Light and Electrons* (Oxford University Press, Oxford, 2004).
- [25] R. Bistritzer and A. H. MacDonald, Moiré butterflies in twisted bilayer graphene, *Phys. Rev. B* **84**, 035440 (2011).
- [26] K. Hejazi, C. Liu, and L. Balents, Landau levels in twisted bilayer graphene and semiclassical orbits, *Phys. Rev. B* **100**, 035115 (2019).
- [27] Y. Sheffer and A. Stern, Chiral magic-angle twisted bilayer graphene in a magnetic field: Landau level correspondence, exact wave functions, and fractional chern insulators, *Phys. Rev. B* **104**, L121405 (2021).
- [28] E. McCann and M. Koshino, The electronic properties of bilayer graphene, *Rep. Prog. Phys.* **76**, 056503 (2013).
- [29] See supplemental material, [URL will be inserted by publisher], for details on HF, ED and magnetic model calculations.
- [30] P. Mai, J. Zhao, T. A. Maier, B. Bradlyn, and P. W. Phillips, Topological phase transition without single particle gap closing in strongly correlated systems, *Phys. Rev. B* **110**, 075105 (2024).
- [31] Y. H. Kwan, J. Yu, J. Herzog-Arbeitman, D. K. Efetov, N. Regnault, and B. A. Bernevig, Moiré fractional chern insulators iii: Hartree-fock phase diagram, magic angle regime for chern insulator states, the role of the moiré potential and goldstone gaps in rhombohedral graphene superlattices (2023), arXiv:2312.11617 [cond-mat.str-el].
- [32] J. Yu, J. Herzog-Arbeitman, Y. H. Kwan, N. Regnault, and B. A. Bernevig, Moiré fractional chern insulators iv: Fluctuation-driven collapse of fcis in multi-band exact diagonalization calculations on rhombohedral graphene (2024), arXiv:2407.13770 [cond-mat.str-el].
- [33] Z. Guo, X. Lu, B. Xie, and J. Liu, Fractional chern insulator states in multilayer graphene moiré superlattices, *Phys. Rev. B* **110**, 075109 (2024).
- [34] N. Marzari and D. Vanderbilt, Maximally localized generalized wannier functions for composite energy bands, *Phys. Rev. B* **56**, 12847 (1997).
- [35] M. Taherinejad, K. F. Garrity, and D. Vanderbilt, Wannier center sheets in topological insulators, *Phys. Rev. B* **89**, 115102 (2014).
- [36] In our finite-size ED data, the neutral gap remains finite at the sampled boundary conditions near the critical point. However, for an interacting finite system a change of the many-body Chern number necessarily implies a topologically protected level crossing (i.e., a closing of the neutral excitation gap) at some twisted boundary condition in parameter space, as proven in Ref. [54]. In this work we do not attempt to locate this specific crossing point, which is why it does not appear explicitly in the spectra shown in Fig. 2(a).
- [37] H. Li and F. D. M. Haldane, Entanglement spectrum as a generalization of entanglement entropy: Identification of topological order in non-abelian fractional quantum hall effect states, *Phys. Rev. Lett.* **101**, 010504 (2008).
- [38] B. A. Bernevig and F. D. M. Haldane, Model fractional quantum hall states and jack polynomials, *Phys. Rev. Lett.* **100**, 246802 (2008).
- [39] N. Regnault, Entanglement spectroscopy and its application to the quantum hall effects, arXiv e-prints (2015).
- [40] B. A. Bernevig and N. Regnault, Thin-torus limit of fractional topological insulators (2012), arXiv:1204.5682 [cond-mat.str-el].
- [41] More stringent evidence to exclude a weak first-order transition or to determine the universality class may require further studies such as infinite-density matrix

- renormalization group (iDMRG) or a dedicated critical field theory [55], which is beyond the scope of this work.
- [42] A. Seidel and K. Yang, Halperin (m, m', n) bilayer quantum hall states on thin cylinders, *Phys. Rev. Lett.* **101**, 036804 (2008).
- [43] S. Bandyopadhyay, G. Ortiz, Z. Nussinov, and A. Seidel, Local two-body parent hamiltonians for the entire jain sequence, *Phys. Rev. Lett.* **124**, 196803 (2020).
- [44] I. A. McDonald and F. D. M. Haldane, Topological phase transition in the $\nu=2/3$ quantum hall effect, *Phys. Rev. B* **53**, 15845 (1996).
- [45] Y. Liu and Z. Zhu, Engineering fractional chern insulators through periodic strain in monolayer graphene and transition metal dichalcogenides, *Phys. Rev. B* **112**, L041123 (2025).
- [46] S. Niu, J. Alicea, D. N. Sheng, and Y. Peng, Quantum anomalous hall effects and emergent $su(2)$ hall ferromagnets at fractional filling of helical trilayer graphene, *Phys. Rev. Lett.* **135**, 146505 (2025).
- [47] J. K. Jain, Composite-fermion approach for the fractional quantum hall effect, *Phys. Rev. Lett.* **63**, 199 (1989).
- [48] B. I. Halperin and J. K. Jain, *Fractional Quantum Hall Effects: New Developments* (WORLD SCIENTIFIC, 2020).
- [49] Usually, electrons favors local orbitals of smaller trg due to larger Fock energy [51]. Nevertheless, smaller value of $\eta = trg - |F|$ naturally reflect this properties when berry curvature is flat.
- [50] For details on computing quantum geometric quantities under a magnetic field, we recommend that readers refer to the Supplementary Material of Ref. [4].
- [51] A. Abouelkomsan, K. Yang, and E. J. Bergholtz, Quantum metric induced phases in moiré materials, *Phys. Rev. Res.* **5**, L012015 (2023).
- [52] Y. Wang, Z. Wang, Y. Xue, M. Song, K. Watanabe, T. Taniguchi, J. Lu, H. Zhou, J. Kang, K. Chang, H. Gao, Y. Jiang, and J. Mao, Spectral signature of fractional chern insulating states in twisted moiré system, Under review.
- [53] H. Liu, R. Perea-Causin, Z. Liu, and E. J. Bergholtz, Topological order without band topology in moiré graphene (2025), arXiv:2510.15027 [cond-mat.mes-hall].
- [54] C. N. Varney, K. Sun, M. Rigol, and V. Galitski, Topological phase transitions for interacting finite systems, *Phys. Rev. B* **84**, 241105 (2011).
- [55] J. Y. Lee, C. Wang, M. P. Zaletel, A. Vishwanath, and Y.-C. He, Emergent multi-flavor qed_3 at the plateau transition between fractional chern insulators: Applications to graphene heterostructures, *Phys. Rev. X* **8**, 031015 (2018).
- [56] N. Bultinck, E. Khalaf, S. Liu, S. Chatterjee, A. Vishwanath, and M. P. Zaletel, Ground state and hidden symmetry of magic-angle graphene at even integer filling, *Phys. Rev. X* **10**, 031034 (2020).
- [57] For technique details on HF calculation with similar set up, we recommend readers also see [31].
- [58] S. Okamoto, N. Mohanta, E. Dagotto, and D. N. Sheng, Topological flat bands in a kagome lattice multiorbital system, *Commun. Phys.* **5**, 198 (2022).

END MATTER

Projected Interaction Hamiltonian.—Together with the interaction terms, the full band-projected Hamiltonian—obtained after diagonalizing the CM model—can be written as [31, 56],

$$H = \sum_{nk} E_{nk} \hat{n}_{n,\mathbf{k}} + \frac{1}{2A} \sum_{\mathbf{q}} V(\mathbf{q}) : \hat{\rho}_{\mathbf{q}} \hat{\rho}_{-\mathbf{q}} :, \quad (\text{A.1})$$

where $\hat{n}_{n,\mathbf{k}} = \sum_{s,\xi} c_{n,\mathbf{k},s,\xi}^\dagger c_{n,\mathbf{k},s,\xi}$ are particle number operator of non-interacting bands E_{nk} , $\hat{\rho}_{\mathbf{q}} = \sum_{\mathbf{k},m,n,\sigma,\xi,\xi'} \langle u_{\mathbf{k}+\mathbf{q},m,s,\xi} | u_{\mathbf{k},n,s',\xi'} \rangle c_{\mathbf{k}+\mathbf{q},m,s,\xi}^\dagger c_{\mathbf{k},n,s',\xi'}$ is the density operator, A is the area of sample, $s = \uparrow, \downarrow$ is spin index, and $V(\mathbf{q}) = \frac{e^2}{2\epsilon q} \tanh(d_{sc}q/2)$, where $\epsilon \approx 4\epsilon_0$ is the dielectric constant of the material, $d_{sc} = 10 \text{ nm}$ is considered as the distance towards the gate. Here, we consider a model with two spin and two valley flavors, including three active conduction and three valence bands per flavor, along with remote band renormalization effects in average scheme [31, 32]. Within this setup [57], the self-consistent HF ground state is found to be spin-valley polarized [29].

In the main text, we utilize ED to compute the many-body ground states through single band projection of Eq. (A.1), along with their many body Chern number (MBC) [29, 58], and employ the PES to identify their topological character. The PES is obtained by tracing out a subset

of particles from the degenerate ground-state manifold and examining the eigenvalue spectrum of the resulting reduced density matrix $\rho_A = \text{Tr}_B \rho$, and $\xi = -2 \log \rho_A$ with $\rho = \frac{1}{D} \sum_D |\Omega_D\rangle \langle \Omega_D|$ is the ground state density matrix. When the spectrum is gapped, the number of low-energy states below the gap provides a robust fingerprint of the topological order, as it precisely follows the expected counting rules characteristic of specific topological phases [37–39].

Phase diagram.—Importantly, the emergent of FCI1 needs specific conditions in tMBG. As depicted in Fig. 4, we present phase diagrams for both types of FCI phases at $\kappa = 0.5$ and $\kappa = 0.7$, evaluated over varying interaction strength based on dielectric constant ϵ_r and perpendicular electric basis V_{pot} . In both cases, stronger interactions and an fine-tune bias $V_{\text{pot}} \sim 50 \text{ meV}$ are required to stabilize the FCI phases. Notably, FCI-1 favors a larger range of area of phase diagram. While competing phases such as Fermi liquid (FL), charge density wave (CDW), and other gapless states can be distinguished in ED by their energy gaps, structural factors and ground-state degeneracies [29].

Halperin-(112) states— To verify that the FCI-1 phase in our work shares the same topological order as the Halperin-(112) state, we employ the Coulomb Hamilto-

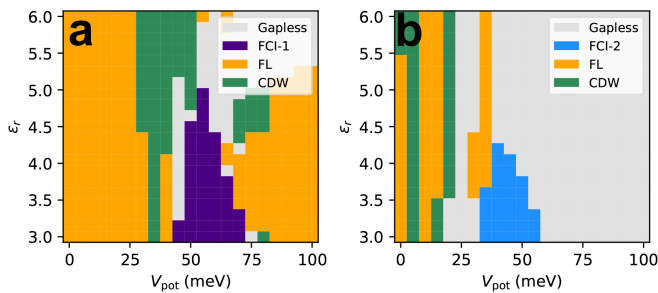


FIG. 4. (a, b) The phase diagram at $\kappa = 0.5$ and $\kappa = 0.7$ in terms of external bias V_{pot} and relative dielectric constant ϵ_r .

nian of Ref. [44], which exhibits nearly unit overlap with the model wave function below,

$$\Psi(z^\uparrow, z^\downarrow) = \mathcal{P}_{LLL} \prod_{i < j} (z_i^{\uparrow*} - z_j^{\uparrow*}) \prod_{i < j} (z_i^{\downarrow*} - z_j^{\downarrow*}) \quad (\text{A.2})$$

$$\times \prod_{i < j} (z_i^\uparrow - z_j^\uparrow)^2 \prod_{i < j} (z_i^\downarrow - z_j^\downarrow)^2 \prod_{i \neq j} (z_i^\uparrow - z_j^\downarrow)^2.$$

Here \mathcal{P}_{LLL} projects onto the lowest Landau level, and z^\uparrow (z^\downarrow) are the complex coordinates of spin-up (spin-down) electrons, where the spin here indicates layer degree of freedom. Although Eq. (A.2) is not the standard form of the Halperin-(112) state, its K matrix and charge vector coincide with those of the standard construction [44], implying the same topological order, i.e.

$$K = K^+ - K^- = \begin{bmatrix} 2 & 2 \\ 2 & 2 \end{bmatrix} - \begin{bmatrix} 1 & 0 \\ 0 & 1 \end{bmatrix} = \begin{bmatrix} 1 & 2 \\ 2 & 1 \end{bmatrix}. \quad \text{In Fig. 5(a)}$$

we diagonalize the Coulomb Hamiltonian [Eq. (50) of Ref. [44]] at layer separation $d = 0$ with 8 electrons and 12 flux quanta, and find a threefold-degenerate ground-state manifold. The PES exhibits the same characteristic counting, with 1520 levels below the entanglement gap, consistent with the same topological order as in our system. These results corroborate that the FCI-1 phase in our system is Halperin-(112)-like.

Hybrid Wannier functions and quantum geometry.— Using single-particle Bloch eigenstates, we construct hybrid Wannier functions (hWFs) that are maximally localized along \hat{x} at fixed k_y [17, 29, 34, 35]. In real space, the hWF is localized along x and extended along y , analogous to Landau-gauge Landau levels; by sweeping k_y we obtain the trajectory of its center $\bar{x}_n(k_y)$ together with its width. Two quantities characterize this evolution: the *center flow* and the *spread*. The slope of the trajectory is set by the Berry curvature, $\frac{d\bar{x}_n(k_y)}{dk_y} = \frac{L_1}{2\pi} \oint_{\text{BZ}_x} dk_x F(\mathbf{k})$, while the spread of the hWF at fixed k_y is quantified by the metric-trace definition we adopt, $w(k_y) \sim \sqrt{L_1 \oint_{\text{BZ}_x} \frac{dk_x}{2\pi} \text{Tr} g(\mathbf{k})}$, consistent with using $\text{tr} g$ to capture the gauge-invariant spread [34]. It follows that for Landau levels or ideal flat bands the hWF trajectory should be a straight line of constant slope and constant width; for the lowest Landau level, the *trace*

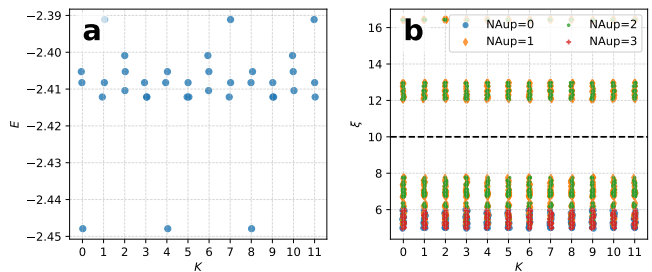


FIG. 5. (a) Energy spectrum of Halperin-(112) FQH states under coulomb interaction with $N_A = 8, N_\phi = 12, S_z = 0$. (b) Corresponding PES which matches (1,2)-counting with $N_A = 3$ for spin up with $S_z = 0, 1, 2, 3$, where 1520 states below the dashed line.

condition $\text{Tr} g(\mathbf{k}) = |F(\mathbf{k})|$ holds, making the slope and the width commensurate along the path [18]. In realistic situations, overly large width implies that electrons are disfavored by exchange from occupying those momenta, thereby raising the local Fock energy; this is captured by the exchange-induced (hole) dispersion [51] $\tilde{\epsilon}_{-\mathbf{k}} \simeq \sum_{\mathbf{q}} V(\mathbf{q}) e^{-g_{ab}(\mathbf{k}) q_a q_b}$, so regions with large $\text{Tr} g(\mathbf{k})$ become exchange-disfavored and are depopulated at HF level, explaining, e.g., the lifting of the HF band near \mathbf{K} and the enhanced dispersion in Fig. 1 (a). In our case, hotspots of Berry curvature manifest as pronounced bends in the hWF trajectories and coincide with peaks of the width; precisely where two $C = 2$ trajectories come close, broader hWFs interfere more strongly and reconnect, providing a transparent picture for the Chern-number-changing topological transition.

Relation with color-entangled ideal flat bands.— Without geometric insatiability, non-ideal flat may be considered adiabatic connecting with its ideal limit. When the flat bands is ideal, one can always choose a normalization factor $\mathcal{N}_{\mathbf{k}}$ to render the wavefunction holomorphic as LLL in non-uniform magnetic field. The color-entangled Bloch wavefunction then typically takes the form: $u_{\mathbf{k}}(\mathbf{r}) = \sum_{\alpha=0}^{C-1} \mathcal{N}_{\mathbf{k}} \mathcal{B}_\alpha(\mathbf{r}) v_{\mathbf{k}}^\alpha(\mathbf{r})$, where $u_{\mathbf{k}}(\mathbf{r})$ is the periodic part of the flat band Bloch wavefunction, $v_{\mathbf{k}}^\alpha(\mathbf{r}) = v_{\mathbf{k}}(\mathbf{r} + \mathbf{a}_\alpha)$ are Landau level-like components labeled by color index α , and $\mathcal{B}_\alpha(\mathbf{r}) = \mathcal{B}(\mathbf{r} + \mathbf{a}_\alpha)$ entangles these components. The normalization factor is given by $\mathcal{N}_{\mathbf{k}} = e^{-C|\mathbf{k}|^2/4} \mathcal{N}_{\mathbf{k}}$, with lattice vectors $\mathbf{a}_\alpha = \sum_{i=1,2} \alpha_i \mathbf{a}_i$, and $\alpha_i = 0, \dots, C_i - 1$ under the gauge choice $C = C_1 \times C_2$, mimicking a dual magnetic translational group (MTG) [8–10]. Note that one of the most difference between color separation and this decomposition in ideal limit is the involving of geometric instability and external driver like interaction and magnetic field. In non-ideal flat bands, the decomposition may have higher Landau level components, akin to the Λ -level picture in composite fermion [48]. Generally, the color separation effect may stabilize FCIs not only in $|C| > 1$ flat bands but also in $|C| = 1$ or trivial non-ideal flat bands [53]

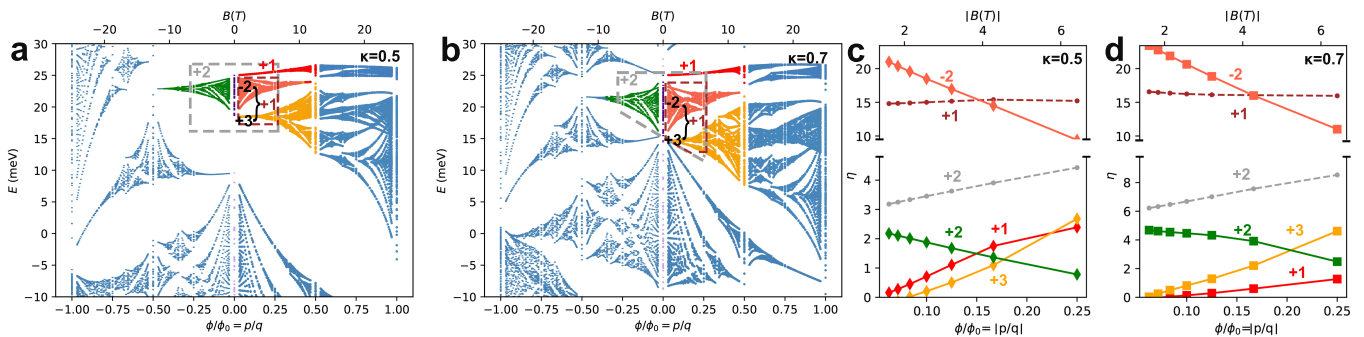


FIG. 6. (a,b) Hofstadter Butterfly at $\kappa = 0.5$ and $\kappa = 0.7$ with $p, q < 20$ for $+K$ valley, where Chern numbers are labeled and can be verified from Diophantine equation of Wannier plot [29]. (c,d) The violation of trace condition variation in terms of magnetic field for magnetic subbands within the box in (a,b) with same color. The dashed line represents η for multi-bands

with non-uniform geometries. Developing a systematic understanding of the color separation effect could significantly enhance our insights into the relationship between quantum geometry and strongly correlated phases.

Stronger magnetic field.—As shown in Fig. 6(a,b), we compute the magnetic spectrum of tMBG at the $+K$ valley (for the $-K$ valley, the magnetic field and Chern numbers are reversed). Under positive magnetic field, the original $C = +2$ flat band splits into subbands with Chern numbers $+1$, -2 , and $+3$. In contrast, under nega-

tive magnetic field, the band remains intact with $C = +2$. We further evaluate the violation of the trace condition for magnetic subbands. Interestingly, at both $\kappa = 0.5$ and $\kappa = 0.7$, the separated subbands (need stronger field, different from color separation effect) with Chern numbers $C = 1$ and $C = 3$ exhibit nearly ideal trace conditions, with $\eta \sim 0.1$. In contrast, only at $\kappa = 0.5$ does the original $C = 2$ band attain $\eta \sim 2$ under a weak negative magnetic field. This means stronger negative field can stabilize Laughlin and Halperin-like states generally.

Supplementary Material for Fractional Chern Insulators Transition in Non-ideal Flat Bands of Twisted Mono-bilayer Graphene

Moru Song^{1,2,3} and Kai Chang^{2,*}

¹State Key Laboratory of Semiconductor Physics and Chip Technologies,
Institute of Semiconductors, Chinese Academy of Sciences, Beijing 100083, China

²Center for Quantum Matter, Zhejiang University, Hangzhou 310027, China

³College of Materials Science and Opto-electronic Technology,
University of Chinese Academy of Sciences, Beijing 100049, China

(Dated: November 25, 2025)

CONTENTS

S1. Hartree Fock calculation	1
A. Dual gate interaction	2
B. Background terms	2
C. Active terms	2
D. Self-consistent Hartree-Fock procedure	3
E. Full Hartree Fock band structure	3
F. Berry curvature near critical point	4
S2. Hybrid Wannier Functions	5
A. Geometry of Hybrid Wannier function	5
B. Relation between real-space hWF width and the trace of the quantum metric	5
S3. Exact Diagonalization results	7
A. Momentum space mesh	7
B. Comparison of FCI-1 and conventional two components Halperin model states	8
C. Admissible-(1, 2) rule in FCI-1	8
D. Key numerical properties of FCI-1 at $\nu = 1/3$	9
E. Additional Exact Diagonalization results	9
F. Calculation details on Particle Entanglement Spectrum	11
G. Calculation of Many body Chern number	11
H. Fidelity diagnostic	11
I. Details on Particle Entanglement Spectrum transition	12
S4. Landau level expansion under magnetic field	13
A. Quantum geometry under magnetic field	13
B. Landau fan of Wannier plot	14
References	15

S1. HARTREE FOCK CALCULATION

In the projected Hartree-Fock (HF) approach, we write the total mean-field Hamiltonian as a sum of single-particle and interaction terms, $\hat{\mathcal{H}}_{\text{HF}} = \hat{\mathcal{H}}_0 + \hat{\mathcal{H}}_{\text{bg}} +$

$\hat{\mathcal{H}}_{\text{int}}[\delta\rho]$. Here $\hat{\mathcal{H}}_0$ is the non-interacting moiré band Hamiltonian (including kinetic energy and any external potential such as interlayer bias), $\hat{\mathcal{H}}_{\text{bg}}$ is the static mean-field due to the **remote bands** (those outside the active window), and $\hat{\mathcal{H}}_{\text{int}}[\delta\rho]$ is the self-consistent interaction term from the **active bands**. Following the scheme of [1, 2], the remote valence bands (fully filled in the non-interacting picture) and remote conduction bands (empty) are treated as an inert background (average scheme [1, 2]): we subtract a reference half-filling for each remote state so that only their deviation (filled $-\frac{1}{2}$ or empty $-\frac{1}{2}$) contributes to a background Hartree-Fock potential. This ensures that the high-energy bands do not explicitly enter the variational HF energy, aside from renormalizing the active bands via a fixed one-body potential. We now define the key tensors entering the HF formulation. First, the umklapp matrix Γ enforces momentum conservation up to a moiré reciprocal lattice vector \mathbf{G} . In an extended plane-wave basis (indexing plane-wave momenta by integers g, g'), $\Gamma_{gg'}(\mathbf{G}) = \delta_{\mathbf{G}_g, \mathbf{G}_{g'} + \mathbf{G}}$. Next, the **form factor tensor** Λ encodes the inter-band overlap of Bloch states upon momentum transfer. In particular, for a given valley ξ and layer l , we define $\Lambda_{mn}^{(\xi,l)}(\mathbf{k}, \mathbf{q} + \mathbf{G})$ as the overlap between an active Bloch state $|u_{n,\mathbf{k}}^{(\xi)}\rangle$ and another state $|u_{m,\mathbf{k}+\mathbf{q}}^{(\xi)}\rangle$ after a momentum boost by $\mathbf{q} + \mathbf{G}$. Writing $U_{n,\mathbf{k}}^{(\xi)}(g, l, \alpha)$ for the plane-wave expansion coefficient of $|u_{n,\mathbf{k}}^{(\xi)}\rangle$ on layer l and sublattice α (with g labeling the moiré reciprocal lattice vectors in the plane-wave cutoff), we have the explicit form factor:

$$\begin{aligned} \Lambda_{mn}^{(\xi,l)}(\mathbf{k}, \mathbf{q} + \mathbf{G}) & \quad (S1) \\ & = \sum_{g_1, g_2, \alpha} U_{m, \mathbf{k}+\mathbf{q}}^{(\xi)*}(g_1, l, \alpha) \Gamma_{g_1 g_2}(\mathbf{G}) U_{n, \mathbf{k}}^{(\xi)}(g_2, l, \alpha), \end{aligned}$$

which is an overlap matrix element between Bloch states at \mathbf{k} and $\mathbf{k} + \mathbf{q}$ with a reciprocal shift \mathbf{G} . This tensor $\Lambda_{mn}^{(\xi,l)}(\mathbf{k}, \mathbf{q} + \mathbf{G})$ carries indices for the initial band n , final band m , valley ξ , layer l , and momenta \mathbf{k} (in the moiré Brillouin zone) and $\mathbf{q} + \mathbf{G}$ (the momentum transfer, decomposed into a small momentum \mathbf{q} in the first moiré Brillouin zone plus a reciprocal lattice vector \mathbf{G} , i.e. an umklapp component).

* kchang@zju.edu.cn

A. Dual gate interaction

In our main text, we use the two dimensional dual gate interaction,

$$V_{L,l}(\mathbf{q}) = \frac{e^2}{2\epsilon q A} \tanh(qd_{sc}), \quad (\text{S2})$$

which is independent of layer. In general, the interaction should layer dependents as given in ref [1]. In the derivation below, we assume the most general cases and write the layer index $L, l = 0, 1, 2$ explicitly. For a layer dependence interaction, one can use $V_{L,l}(\mathbf{q})$ in [1],

B. Background terms

Using the form factors, we can express the **background density matrix** due to remote bands. Let $f_{m,\xi}$ be the occupation of remote band m in valley ξ (so $f_{m,\xi} = 1$ for filled remote valence bands, 0 for empty remote conduction bands). The reference subtraction scheme sets each remote $f_{m,\xi}^{\text{ref}} = \frac{1}{2}$, so the net background occupancy is $\delta f_{m,\xi} = f_{m,\xi} - \frac{1}{2} = \pm \frac{1}{2}$. The Fourier-component of the background charge density on layer l at momentum \mathbf{G} is then

$$\mathcal{N}_l^{\text{bg}}(\mathbf{G}) = \frac{1}{N_{\text{cell}}} \sum_{\xi} \sum_{m \in \text{remote}} \sum_{\mathbf{k}} \left(f_{m,\xi} - \frac{1}{2} \right) \Lambda_{mm}^{(\xi,l)}(\mathbf{k}, \mathbf{G}), \quad (\text{S3})$$

where N_{cell} is the number of moiré unit cells in the periodic HF supercell (so that $\frac{1}{N_{\text{cell}}} \sum_{\mathbf{k}}$ indicates an average over the moiré Brillouin zone). In Eq. (S3), $\Lambda_{mm}(\mathbf{k}, \mathbf{G})$ is the intra-band form factor giving the weight of Bloch state m at wavevector \mathbf{k} on layer l with momentum transfer \mathbf{G} ; thus $\mathcal{N}_l^{\text{bg}}(\mathbf{G})$ represents the Fourier-space density (relative to the neutralizing reference) contributed by all remote bands on layer l . In particular, $\mathcal{N}_l^{\text{bg}}(0)$ yields the total background charge in layer l , while nonzero \mathbf{G} components encode the periodic charge modulation from remote-band Bloch states.

We can now write the HF mean-field Hamiltonian acting within the active subspace. The **background Hartree-Fock term** $\hat{\mathcal{H}}_{\text{bg}}$ is a one-body operator representing the static Coulomb field of the remote-band charges (both Hartree direct and Fock exchange) felt by the active electrons. It can be expressed as

$$[H_{\text{bg}}]_{nn'}(\mathbf{k}) = [H_{\text{bg}}^H]_{nn'}(\mathbf{k}) + [H_{\text{bg}}^F]_{nn'}(\mathbf{k}), \quad (\text{S4})$$

with separate contributions from the Hartree (H) and Fock (F) parts. In the Hartree (direct) term H_{bg}^H , the active electrons on layer L experience an electrostatic potential from the background charge in layer l . In Fourier space this is given by the Coulomb interaction $V_{Ll}(\mathbf{G})$ between a charge on layer L and a charge on layer l at relative momentum \mathbf{G} . Thus, using the background density $\mathcal{N}_l^{\text{bg}}$ defined above, we have

$$[H_{\text{bg}}^H]_{nn'}(\mathbf{k}) = \sum_{L,l} \sum_{\mathbf{G}} V_{Ll}(\mathbf{G}) \Lambda_{nn'}^{(\xi,L)}(\mathbf{k}, \mathbf{G}) \mathcal{N}_l^{\text{bg}}(-\mathbf{G}), \quad (\text{S5})$$

where $\Lambda_{nn'}^{(\xi,L)}(\mathbf{k}, \mathbf{G})$ serves as a form-factor projector of the active nn' state (at valley ξ) onto layer L for the plane-wave component $e^{i\mathbf{G}\cdot\mathbf{r}}$, and $\mathcal{N}_l^{\text{bg}}(-\mathbf{G})$ is the background charge on layer l with the opposite momentum $-\mathbf{G}$ (ensuring overall momentum conservation in the Hartree term). Equation (S5) shows that a nonzero $\mathcal{N}_l^{\text{bg}}(\mathbf{G})$ (coming from remote-band charge imbalance) generates a Hartree potential acting on the active bands via their form factors $\Lambda_{nn'}$. Meanwhile, the **Fock term** H_{bg}^F represents the exchange self-energy contributed by the filled remote bands. An active electron in band n' can virtually exchange with an electron in a remote band m (valence) or a hole in a remote band m (conduction) of the same valley, resulting in a correction to the one-body energy of the active state n' . Using the form factors to handle wavefunction overlaps, we write the background Fock contribution as

$$[H_{\text{bg}}^F]_{nn'}(\mathbf{k}) = - \sum_{L,l} \sum_{\mathbf{q}, \mathbf{G}} \frac{V_{Ll}(\mathbf{q} + \mathbf{G})}{N_{\text{cell}}} \times \sum_{m \in \text{remote}} \delta f_{m,\xi} \Lambda_{nm}^{(\xi,L)}(\mathbf{k}, \mathbf{q} + \mathbf{G}) \Lambda_{m n'}^{(\xi,l)}(\mathbf{k} + \mathbf{q}, -\mathbf{q} - \mathbf{G}), \quad (\text{S6})$$

where $V_{Ll}(\mathbf{q} + \mathbf{G})$ is the interlayer Coulomb interaction at momentum $\mathbf{q} + \mathbf{G}$, and the product of two Λ tensors arises from the two exchange vertices: an active electron n at \mathbf{k} scatters into a remote state m at $\mathbf{k} + \mathbf{q}$ (via $\Lambda_{nm}^{(\xi,L)}$ on layer L) and then back to an active state n' at \mathbf{k} (via $\Lambda_{m n'}^{(\xi,l)}$ on layer l after exchanging momentum $\mathbf{q} + \mathbf{G}$). The factor $(f_{m,\xi} - \frac{1}{2}) = \pm \frac{1}{2}$ weights the contribution of each remote band m depending on whether it is filled or empty (remote valence or conduction). We emphasize that $\hat{\mathcal{H}}_{\text{bg}}$ is a static one-body Hamiltonian (a sum of layer-dependent potentials and exchange self-energies) that is fixed by the remote-band configuration and does not depend on the active-state occupations $\delta\rho$. In practice this $\hat{\mathcal{H}}_{\text{bg}}$ provides an effective **background HF potential** (sometimes called the “reference” or “subtraction” potential: that renormalizes the energies of the active bands.

C. Active terms

Finally, the term $\hat{\mathcal{H}}_{\text{int}}[\delta\rho]$ represents the interaction corrections from the active subspace itself. It is a functional of the active electron density matrix $\rho_{nn'}$. We may similarly decompose it into Hartree and Fock pieces:

$$[H_{\text{int}}[\delta\rho]]_{nn'}(\mathbf{k}) = [H_{\text{int}}^H[\delta\rho]]_{nn'}(\mathbf{k}) + [H_{\text{int}}^F[\delta\rho]]_{nn'}(\mathbf{k}), \quad (\text{S7})$$

where $\delta\rho_{mn}(\mathbf{k}, \xi, s) = \rho_{mn}(\mathbf{k}, \xi, s) - \frac{1}{2}\mathbb{I}$ is the relative density matrix. Here, $s = \uparrow, \downarrow$ represent spin degree of

freedom. This kind representation of density matrix imply we neglect the spin, valley and momentum coherence. For the active Hartree terms, we have

$$[H_{\text{int}}^H[\delta\rho]]_{nn'}(\mathbf{k}, \xi, s) = \sum_{\mathbf{G}, Ll} V_{Ll}(\mathbf{G}) \Lambda_{nn'}^{(\xi, L)}(\mathbf{k}, \mathbf{G}) \mathcal{N}_l^{\text{act}}[\delta\rho] \quad (\text{S8})$$

where

$$\mathcal{N}_l^{\text{act}} = \frac{1}{N_{\text{cell}}} \sum_{\mathbf{q}, \xi', s'} \sum_{m, m'} \Lambda_{mm'}^{(\xi', l)}(\mathbf{k}', -\mathbf{G}) \delta\rho_{m'm}(\mathbf{k}', \xi', s') \quad (\text{S9})$$

is the self-consistent charge on layer l that is contributed from active bands. The Fock term is written,

$$\begin{aligned} [H_{\text{int}}^F[\delta\rho]]_{nn'}(\mathbf{k}, \xi, s) &= - \sum_{\mathbf{q}, \mathbf{G}, Ll} \frac{V_{Ll}(\mathbf{q} + \mathbf{G})}{N_{\text{cell}}} \quad (\text{S10}) \\ &\times \sum_{m, m'} \Lambda_{m, n}^{(\xi, l)}(\mathbf{k} + \mathbf{q}, -\mathbf{q} - \mathbf{G}) \Lambda_{m', n'}^{(\xi, L)}(\mathbf{k}, \mathbf{q} + \mathbf{G}) \\ &\times \delta\rho_{m'm}(\mathbf{k} + \mathbf{q}, \xi, s), \end{aligned}$$

In summary, the mean-field Hamiltonian for twisted moiré Bernal graphene (tMBG) is constructed as $\hat{\mathcal{H}}_{\text{HF}} = \hat{\mathcal{H}}_0 + \hat{\mathcal{H}}_{\text{bg}} + \hat{\mathcal{H}}_{\text{int}}[\delta\rho]$, comprising the single-particle term $\hat{\mathcal{H}}_0$, the background HF potential $\hat{\mathcal{H}}_{\text{bg}}$ from remote bands (valence and conduction treated via a half-filling reference as in [1]), and the interaction corrections $\hat{\mathcal{H}}_{\text{int}}[\delta\rho]$

arising from the active bands' density matrix. The tensors Γ , Λ , and $\mathcal{N}_l^{\text{bg}}$ defined in Eqs. (S1)–(S3) encapsulate the moiré form factors and background charge needed to evaluate the Hartree–Fock matrix elements in Eqs. (S5)–(S10). This formalism cleanly separates the static renormalization from remote bands (encoded in $\hat{\mathcal{H}}_{\text{bg}}$) and the self-consistent interactions within the active bands (encoded in $\hat{\mathcal{H}}_{\text{int}}[\delta\rho]$), providing a clear framework for implementing the HF mean-field Hamiltonian of tMBG.

D. Self-consistent Hartree-Fock procedure

Our self-consistent HF workflow begins with the computation of the form factors associated with each valley. For a given valley, the form factors are classified into two categories based on the band indices: (i) inter-band form factors between the remote bands and the active bands, and (ii) intra-band form factors within the active bands themselves. In our calculations, we designate three conduction bands and three valence bands as the active bands. Subsequently, we compute the background Hamiltonian. For completeness and numerical stability, we include all bands in the CM model in this stage. Next, we calculate and storage the Hartree and Fock interaction tensors, denoted respectively as $V_{\xi, \mathbf{k}, n, n'; \xi', \mathbf{k}', m', m}^H$ and $V_{\xi, \mathbf{k}, n, n'; \mathbf{q}, m, m'}^F$, which satisfied.

$$[H_{\text{int}}^H[\delta\rho]]_{nn'}(\mathbf{k}, \xi, s) = \sum_{\xi', \mathbf{k}', s', m', m} V_{\xi, \mathbf{k}, n, n'; \xi', \mathbf{k}', m', m}^H \delta\rho_{m'm}(\mathbf{k}', \xi', s') \quad (\text{S11})$$

$$[H_{\text{int}}^F[\delta\rho]]_{nn'}(\mathbf{k}, \xi, s) = - \sum_{\mathbf{q}, m, m'} V_{\xi, \mathbf{k}, n, n'; \mathbf{q}, m, m'}^F \delta\rho_{m'm}(\mathbf{k} + \mathbf{q}, \xi, s') \quad (\text{S12})$$

as defined in Eq. (S11)–(S12). These tensors serve as the effective interactions in the HF Hamiltonian and are treated as fixed input data during the self-consistency loop.

With the interaction tensors fixed, we iteratively solve for the density matrix $\rho_{m, m'}$ until convergence is achieved, following the standard self-consistent Hartree-Fock procedure.

$$\rho_{nn'}^{(i)}(\mathbf{k}, \xi, s) = \sum_{\alpha \in \text{occ}(\xi, s)} V_{\alpha, n}^{(i)}(\mathbf{k}, \xi) V_{\alpha, n'}^{(i)\dagger}(\mathbf{k}, \xi) \quad (\text{S13})$$

where $V_{\alpha, n}^{(i)}(\mathbf{k}, \xi)$ is the eigenvector of HF Hamiltonian within the i th step iteration, α is sum over the occupied orbitals. In our spin-valley polarized set up at filling $\nu = 1$, we separately occupy each $(\xi, s) = (K, \uparrow), (K, \downarrow), (K', \uparrow), (K', \downarrow)$ sectors with $3 + 1, 3 + 0, 3 + 0, 3 + 0$

active bands for each k-points.

E. Full Hartree Fock band structure

In this section, we present the fully spin-valley-polarized band structures at $\kappa = 0.5$ and $\kappa = 0.7$. As illustrated in Fig. S1(e), these calculations are performed on a 12×12 momentum mesh within the first Brillouin zone (BZ). For comparison, Figs. S1(b) and (d) display the corresponding Berry curvature distributions. At $\kappa = 0.5$, the Berry curvature of the target conduction bands remains strictly negative throughout the entire BZ, whereas at $\kappa = 0.7$, the Berry curvature exhibits nodes and changes sign, resulting in a net cancellation within the BZ. Consistent with the results presented in

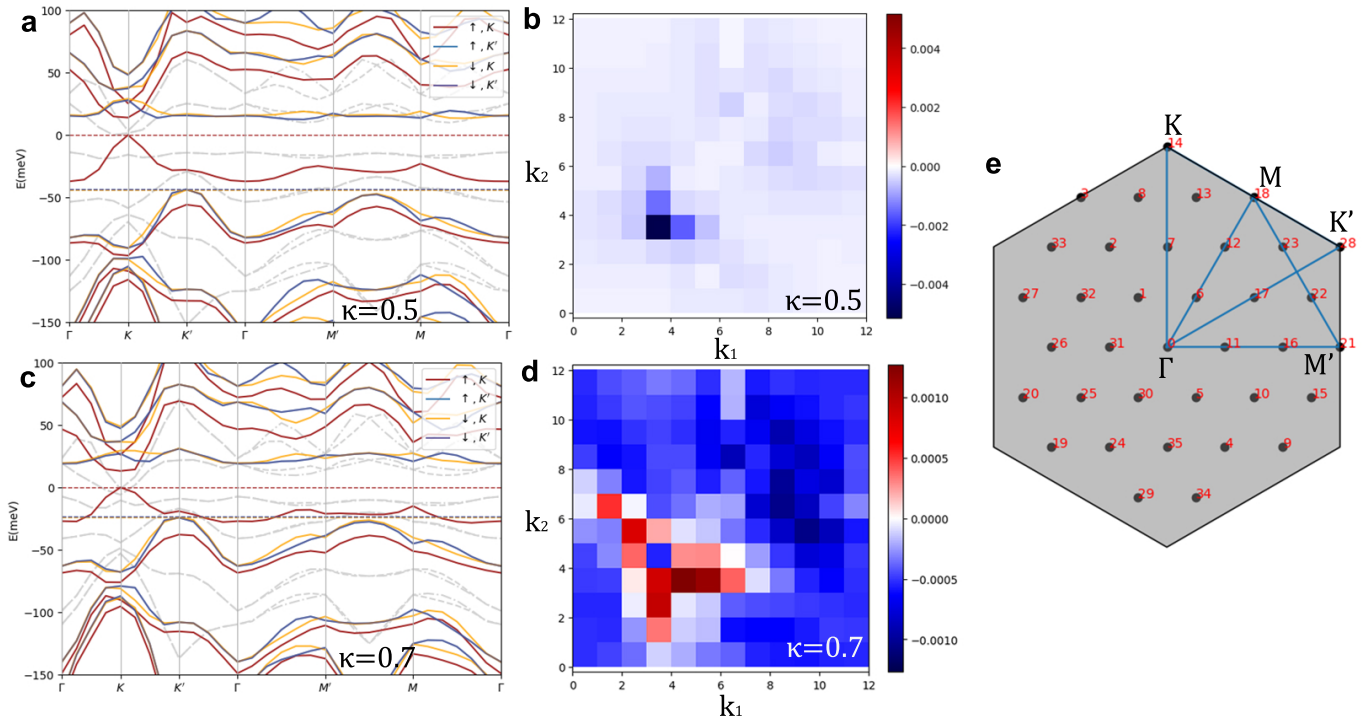


FIG. S1. (a,c) Spin-valley polarized Hartree Fock bands on $N_1 \times N_2 = 12 \times 12$ mesh, the dashed colored line label the maximum filling of corresponding favor, the gray dashed line represent non-interacting bands. (b, d) Berry curvature distribution of target flat bands, the colorbar labels $F/2\pi N_1 N_2$. (e) The momentum space mesh for HF calculation, the path along high symmetry points are illustrate, where the path points are labeled with $N_1 k_2 + k_1$.

the main text, the variance of the Berry curvature for the two cases is found to be 0.17 and 0.08, respectively, while the associated Chern numbers of the target conduction bands are $C = 2$ and $C = 1$. The deviations from the trace condition are found to be $\eta = 6.8$ and $\eta = 9.6$ for $\kappa = 0.5$ and $\kappa = 0.7$, respectively. Compared to the corresponding non-interacting values of $\eta = 4.2$ and $\eta = 6.3$, this indicates a further departure from the ideal flat-band limit at the Hartree-Fock level. Notably, when accounting for all spin and valley flavors, the interaction clearly favors a single spin-valley polarization near the Fermi level—specifically, the (K, \uparrow) sector—which supports the validity of the single-band projection employed in our ED calculations. Furthermore, since the interactions separate the bands of different spins and valleys, a typical orbital ferromagnetism develops, leading to spontaneous breaking of time-reversal symmetry.

F. Berry curvature near critical point

In usual single particle Hamiltonian, the transition of Chern number must experience a band touching process at critic point. However, the change of Chern number here is spontaneous, which do not need a single particle band gap closing, but rather close neutral energy gap. In Fig. S2, we scan parameter κ near κ_c at Hatree-Fock level to explicit show this phenomenon. One key properties is

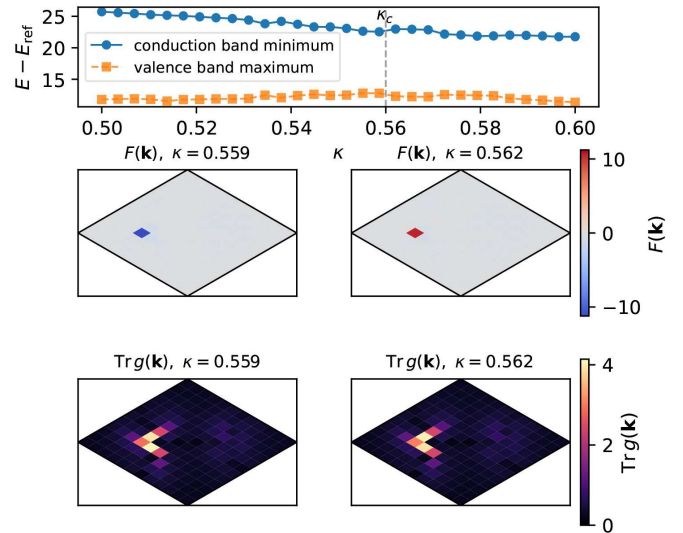


FIG. S2. Upmost: Topological transition without band gap closing. Lower: Berry curvature and metric trace near critical point under HF approximation.

the berry curvature reverse sign suddenly after transition near K points, which is very different from topological phase transition in a band insulator.

S2. HYBRID WANNIER FUNCTIONS

The hybrid Wannier function (hWF) needs an extra k_x -dependent phase to enforce the parallel-transport gauge along \hat{x} (so that the state is maximally localized in x). The corrected single-band expression at fixed k_y is

$$|W_{nX}(k_y)\rangle = \frac{L_1}{2\pi} \oint_{\text{BZ}_x} dk_x e^{-ik_x X L_1} \times \exp\left[-i \int_0^{k_x} dk'_x (A_x^{(n)}(k'_x, k_y) - \bar{A}_x^{(n)}(k_y))\right] |\psi_{n\mathbf{k}}\rangle, \quad (\text{S14})$$

where

$$\begin{aligned} A_x^{(n)}(\mathbf{k}) &= i\langle u_{n\mathbf{k}} | \partial_{k_x} u_{n\mathbf{k}} \rangle, & (\text{S15}) \\ \bar{A}_x^{(n)}(k_y) &= \frac{1}{2\pi/L_1} \oint_{\text{BZ}_x} dk_x A_x^{(n)}(\mathbf{k}) = \frac{\phi_n(k_y)}{L_1}, & (\text{S16}) \\ \bar{x}_n(k_y) &= \frac{L_1}{2\pi} \phi_n(k_y), \quad e^{i\phi_n(k_y)} = \text{eig } \mathcal{W}_x(k_y). & (\text{S17}) \end{aligned}$$

The factor $\exp[-i \int^{k_x} (A_x - \bar{A}_x) dk'_x]$ removes the longitudinal Berry-connection fluctuations along k_x (up to the constant average \bar{A}_x), i.e. imposes the parallel-transport gauge, which is the condition that guarantees maximal localization along x .

A. Geometry of Hybrid Wannier function

In real space we define the hybrid Wannier wave function by

$$\psi_{nX}(x, y; k_y) = \langle x, y | W_{nX}(k_y) \rangle. \quad (\text{S18})$$

In the plane-wave representation used in the numerics, this can be written schematically as

$$\psi_{nX}(x, y; k_y) = \sum_{G=(g,h)} c_{X,G}^{(n)}(k_y) e^{i2\pi[gx + (h+k_y^{\text{frac}})y]}, \quad (\text{S19})$$

where $G = (g, h)$ are integer reciprocal-lattice indices, $k_y^{\text{frac}} = k_y L_2 / 2\pi$ is the reduced crystal momentum along \hat{y} , and the coefficients $c_{X,G}^{(n)}(k_y)$ are obtained from the Bloch eigenstates $|u_{n\mathbf{k}}\rangle$ by a discrete Fourier transform in k_x combined with the parallel-transport gauge fixing.

The corresponding probability density in real space is

$$\rho_{nX}(x, y; k_y) = |\psi_{nX}(x, y; k_y)|^2, \quad (\text{S20})$$

which is normalized as

$$\int dx \int dy \rho_{nX}(x, y; k_y) = 1. \quad (\text{S21})$$

(On a discrete grid $\{x_j, y_i\}$ with spacings $\Delta x, \Delta y$, the normalization condition becomes $\sum_{i,j} \rho_{nX}(x_j, y_i; k_y) \Delta x \Delta y = 1$.)

In Figure S3, we plot the real-space distribution of the hWF of the target band at different k_y . In principle, we can define its x -direction width using the marginal density

$$\rho^{(x)}(x; k_y) = \int dy \rho_{nX}(x, y; k_y), \quad (\text{S22})$$

and the corresponding center

$$\mu(k_y) = \frac{\int dx x \rho^{(x)}(x; k_y)}{\int dx \rho^{(x)}(x; k_y)}. \quad (\text{S23})$$

In the parallel-transport gauge, $\mu(k_y)$ coincides with the Wannier center $\bar{x}_n(k_y)$ extracted from the Wilson loop, up to the integer cell index X .

For this single target band, we denote the x -direction standard deviation of the hybrid Wannier function by $w(k_y)$. It is defined as

$$w^2(k_y) = \frac{\int dx (x - \mu(k_y))^2 \rho^{(x)}(x; k_y)}{\int dx \rho^{(x)}(x; k_y)}, \quad (\text{S24})$$

and

$$w(k_y) = \sqrt{w^2(k_y)}. \quad (\text{S25})$$

On the discrete real-space grid used in the calculation, Eq. (S24) is implemented as

$$\rho^{(x)}(x_j; k_y) = \sum_i \rho_{nX}(x_j, y_i; k_y) \Delta y, \quad (\text{S26})$$

$$\mu(k_y) = \frac{\sum_j x_j \rho^{(x)}(x_j; k_y) \Delta x}{\sum_j \rho^{(x)}(x_j; k_y) \Delta x}, \quad (\text{S27})$$

$$w^2(k_y) = \frac{\sum_j (x_j - \mu(k_y))^2 \rho^{(x)}(x_j; k_y) \Delta x}{\sum_j \rho^{(x)}(x_j; k_y) \Delta x}, \quad (\text{S28})$$

which directly corresponds to the numerical procedure used to extract $w(k_y)$ from the real-space density $\rho_{nX}(x, y; k_y)$.

B. Relation between real-space hWF width and the trace of the quantum metric

To connect the real-space width $w(k_y)$ defined in Eq. (S24) to the band quantum geometry, we recall that for a single isolated band n the quantum geometric tensor of the cell-periodic Bloch state $|u_{n\mathbf{k}}\rangle$ is

$$Q_{\mu\nu}^{(n)}(\mathbf{k}) = \langle \partial_{k_\mu} u_{n\mathbf{k}} | (1 - |u_{n\mathbf{k}}\rangle \langle u_{n\mathbf{k}}|) | \partial_{k_\nu} u_{n\mathbf{k}} \rangle, \quad (\text{S29})$$

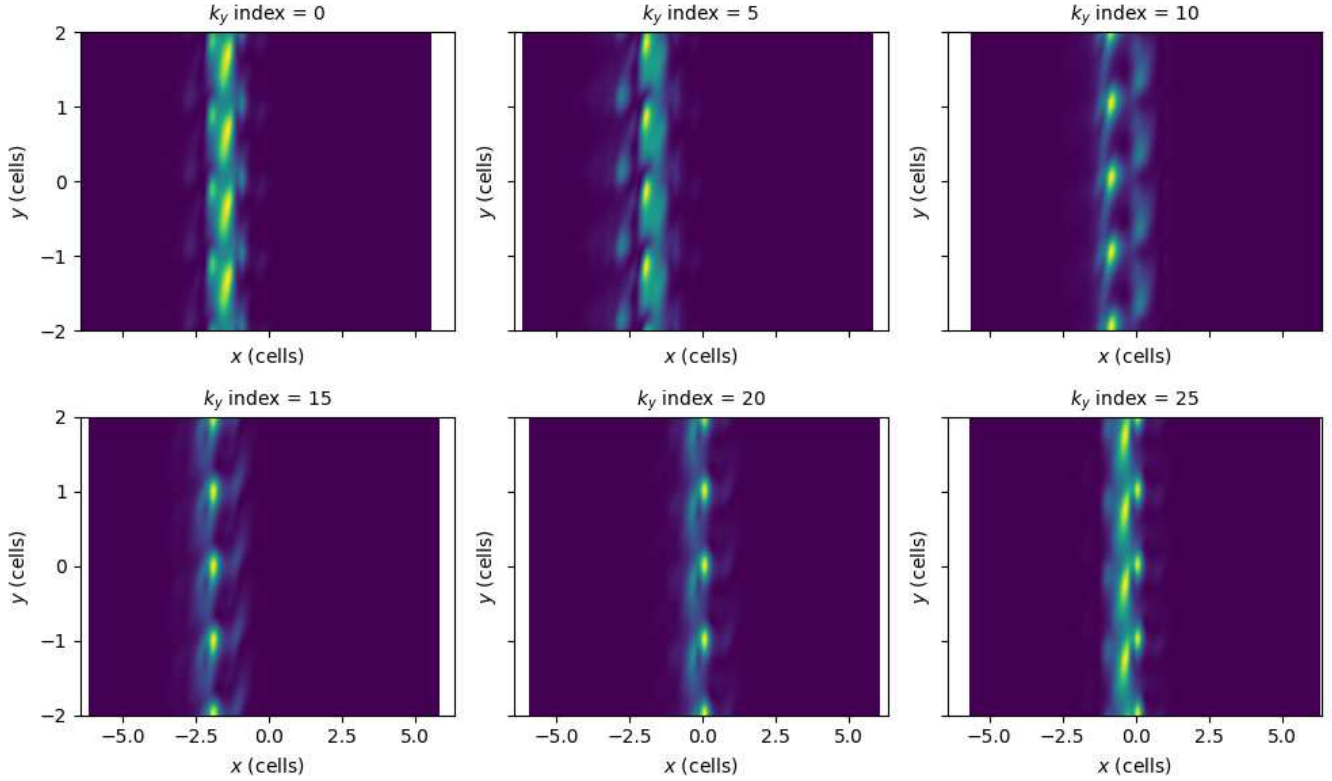


FIG. S3. Hybrid Wannier functions distribution for $\kappa = 0.64$ in real space at different k_y , where the k_y index from 0 to 30 indicates the path along $\Gamma - K - M - K' - \Gamma$.

whose real part defines the quantum metric

$$g_{\mu\nu}^{(n)}(\mathbf{k}) = \text{Re} Q_{\mu\nu}^{(n)}(\mathbf{k}). \quad (\text{S30})$$

In particular, for the x -direction we have

$$g_{xx}^{(n)}(\mathbf{k}) = \langle \partial_{k_x} u_{n\mathbf{k}} | \partial_{k_x} u_{n\mathbf{k}} \rangle - |\langle u_{n\mathbf{k}} | \partial_{k_x} u_{n\mathbf{k}} \rangle|^2, \quad (\text{S31})$$

and in two dimensions the trace of the metric is

$$\text{Tr} g^{(n)}(\mathbf{k}) = g_{xx}^{(n)}(\mathbf{k}) + g_{yy}^{(n)}(\mathbf{k}). \quad (\text{S32})$$

At fixed k_y , the width $w^2(k_y)$ defined in Eq. (S24) is simply the variance of the position operator \hat{x} in the hybrid Wannier state $|W_{nX}(k_y)\rangle$:

$$w^2(k_y) = \langle \hat{x}^2 \rangle_{k_y} - \langle \hat{x} \rangle_{k_y}^2, \quad (\text{S33})$$

with expectation values taken in $|W_{nX}(k_y)\rangle$. This form is equivalent to Eq. (S24) once the marginal density (S22) and the center (S23) are used.

To relate this variance to the quantum metric, it is convenient to rewrite $|W_{nX}(k_y)\rangle$ in k_x -space. From Eq. (S14) we introduce the total parallel-transport phase

$$e^{-i\theta_n(k_x, k_y)} := \exp \left[-i \int_0^{k_x} dk'_x (A_x^{(n)}(k'_x, k_y) - \bar{A}_x^{(n)}(k_y)) \right], \quad (\text{S34})$$

and define

$$|f(k_x; k_y)\rangle = e^{-i\theta_n(k_x, k_y)} |u_{n\mathbf{k}}\rangle. \quad (\text{S35})$$

Using $|\psi_{n\mathbf{k}}\rangle = e^{i\mathbf{k}\cdot\hat{\mathbf{r}}} |u_{n\mathbf{k}}\rangle$ and focusing on the x -direction, Eq. (S14) can then be written as

$$|W_{nX}(k_y)\rangle = \frac{L_1}{2\pi} \oint_{\text{BZ}_x} dk_x e^{-ik_x X L_1} e^{ik_x \hat{x}} |f(k_x; k_y)\rangle. \quad (\text{S36})$$

Using the identity

$$\hat{x} e^{ik_x \hat{x}} = i \partial_{k_x} (e^{ik_x \hat{x}}), \quad (\text{S37})$$

and integrating by parts over the periodic Brillouin zone (so that boundary terms vanish), one finds the standard relations (for fixed k_y)

$$\begin{aligned} \langle \hat{x} \rangle_{k_y} &= \langle W_{nX}(k_y) | \hat{x} | W_{nX}(k_y) \rangle \\ &= \frac{L_1}{2\pi} \oint_{\text{BZ}_x} dk_x i \langle f | \partial_{k_x} f \rangle, \end{aligned} \quad (\text{S38})$$

$$\begin{aligned} \langle \hat{x}^2 \rangle_{k_y} &= \langle W_{nX}(k_y) | \hat{x}^2 | W_{nX}(k_y) \rangle \\ &= \frac{L_1}{2\pi} \oint_{\text{BZ}_x} dk_x \langle \partial_{k_x} f | \partial_{k_x} f \rangle. \end{aligned} \quad (\text{S39})$$

Thus the variance can be written as

$$w^2(k_y) = \frac{L_1}{2\pi} \oint_{\text{BZ}_x} dk_x \left[\langle \partial_{k_x} f | \partial_{k_x} f \rangle - |i \langle f | \partial_{k_x} f \rangle|^2 \right]. \quad (\text{S40})$$

Equation (S40) is valid in any gauge. For a *single* isolated band we can now choose a gauge where $\langle u_{n\mathbf{k}} | \partial_{k_x} u_{n\mathbf{k}} \rangle$ is purely imaginary, and the parallel-transport phase $\theta_n(k_x, k_y)$ is chosen such that

$$i \langle f(k_x; k_y) | \partial_{k_x} f(k_x; k_y) \rangle = \bar{A}_x^{(n)}(k_y) \quad (\text{S41})$$

is a k_x -independent constant, equal to the k_x -averaged Berry connection (the same $\bar{A}_x^{(n)}(k_y)$ that appears in the definition of the hWF). In this gauge

$$\partial_{k_x} |f\rangle = e^{-i\theta_n} (\partial_{k_x} - iA_x^{(n)}(\mathbf{k}) + i\bar{A}_x^{(n)}(k_y)) |u_{n\mathbf{k}}\rangle, \quad (\text{S42})$$

and a short algebra gives

$$\begin{aligned} & \langle \partial_{k_x} f | \partial_{k_x} f \rangle - |i \langle f | \partial_{k_x} f \rangle|^2 \\ &= \langle \partial_{k_x} u_{n\mathbf{k}} | \partial_{k_x} u_{n\mathbf{k}} \rangle - |\langle u_{n\mathbf{k}} | \partial_{k_x} u_{n\mathbf{k}} \rangle|^2 = g_{xx}^{(n)}(\mathbf{k}), \end{aligned} \quad (\text{S43})$$

where we used the definition (S31) of the quantum metric component $g_{xx}^{(n)}$. Plugging this back into Eq. (S40), we obtain the key relation

$$w^2(k_y) = \frac{L_1}{2\pi} \oint_{\text{BZ}_x} dk_x g_{xx}^{(n)}(k_x, k_y). \quad (\text{S44})$$

That is, for the hybrid Wannier function constructed in the parallel-transport gauge, the real-space variance along \hat{x} at fixed k_y is exactly the k_x -average of the quantum metric component g_{xx} .

If we further average $w^2(k_y)$ over k_y , we obtain

$$\overline{w^2} := \frac{L_2}{2\pi} \oint_{\text{BZ}_y} dk_y w^2(k_y) \quad (\text{S45})$$

$$= \frac{L_1 L_2}{(2\pi)^2} \int_{\text{BZ}} d^2 k g_{xx}^{(n)}(\mathbf{k}), \quad (\text{S46})$$

while a natural ‘‘trace-metric’’ measure of the band geometry is

$$\begin{aligned} w_{\text{trg}}^2 &:= \frac{L_1 L_2}{(2\pi)^2} \int_{\text{BZ}} d^2 k \text{Tr} g^{(n)}(\mathbf{k}) \\ &= \frac{L_1 L_2}{(2\pi)^2} \int_{\text{BZ}} d^2 k [g_{xx}^{(n)}(\mathbf{k}) + g_{yy}^{(n)}(\mathbf{k})]. \end{aligned} \quad (\text{S47})$$

Since the quantum metric is positive semidefinite, $g_{xx}^{(n)}(\mathbf{k}) \leq \text{Tr} g^{(n)}(\mathbf{k})$ for all \mathbf{k} , and therefore

$$\overline{w^2} \leq w_{\text{trg}}^2, \quad (\text{S48})$$

with equality when the metric is isotropic, $g_{xx}^{(n)}(\mathbf{k}) = g_{yy}^{(n)}(\mathbf{k})$ everywhere in the Brillouin zone. Thus, in the single-band case the hWF variance $w(k_y)$ provides a real-space realization of the band quantum geometry encoded in the quantum metric, and its Brillouin-zone average is directly controlled by the trace of the quantum metric.

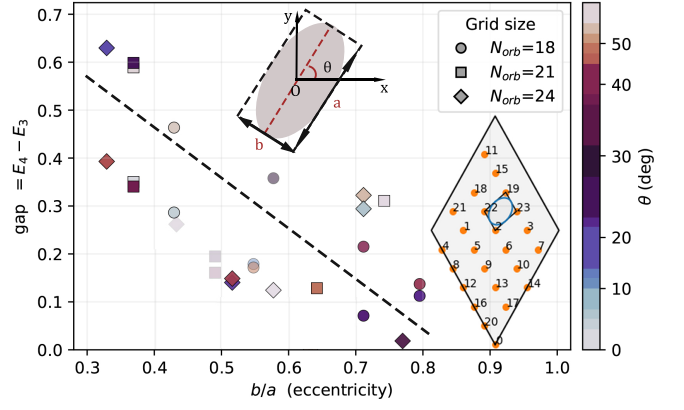


FIG. S4. Variation of ED gap at $\kappa = 0.5$ with respect to different momentum-space meshes. Inset: Illustration of a representative mesh at $b/a = 0.71$, $\theta = 53.1^\circ$. The anisotropy of each mesh is characterized by the eccentricity of the inscribed ellipse within its minimal parallelogram unit.

S3. EXACT DIAGONALIZATION RESULTS

A. Momentum space mesh

For each twist angle we start from the two primitive moiré reciprocal-lattice vectors $\mathbf{b}_{M,1}$, $\mathbf{b}_{M,2}$ ($|\mathbf{b}_{M,1}| = |\mathbf{b}_{M,2}|$, 60°). A momentum mesh is specified by an integer pair (N_1, N_2) —the numbers of grid points sampled along the two primitive directions—and by an $SL(2, \mathbb{Z})$ matrix

$$\tilde{M} = \begin{pmatrix} \tilde{n}_{11} & \tilde{n}_{12} \\ \tilde{n}_{21} & \tilde{n}_{22} \end{pmatrix}, \quad |\det \tilde{M}| = 1. \quad (\text{S49})$$

The rows of \tilde{M} generate a tilted basis $\mathbf{f}_{1,2} = \tilde{n}_{1,2;1} \mathbf{b}_{M,1} + \tilde{n}_{1,2;2} \mathbf{b}_{M,2}$ that spans exactly the same Brillouin zone, but reshapes the rectangular $N_1 \times N_2$ mesh into a general parallelogram. Every crystal momentum is then labeled by the integer pair

$$\begin{aligned} \mathbf{k}(k_x, k_y) &= \frac{k_x}{N_1} \mathbf{f}_1 + \frac{k_y}{N_2} \mathbf{f}_2, \\ k_x &= 0, \dots, N_1 - 1, \quad k_y = 0, \dots, N_2 - 1, \end{aligned} \quad (\text{S50})$$

The parallelogram defined by $\mathbf{f}_{1,2}$ encloses the minimal translational unit of the mesh. To characterize its anisotropy we inscribe the John in-ellipse of that parallelogram and record its semi-axes $a \geq b$ and the orientation θ of the major axis. The ratio $b/a \leq 1$ serves as a dimensionless measure of anisotropy: $b/a \simeq 1$ corresponds to an essentially isotropic mesh, whereas smaller b/a signals a more elongated, strongly anisotropic sampling.

At smaller values of κ , the system is in Halperin (112) like-FCI phase. We find the anisotropy of mesh have great influence on the gap of such FCI states, which may brings anisotropy to computed ground states. To be specific, as illustrate in Fig. S4, FCI gap shrink at more isotropic choice of mesh. In particular, we construct a

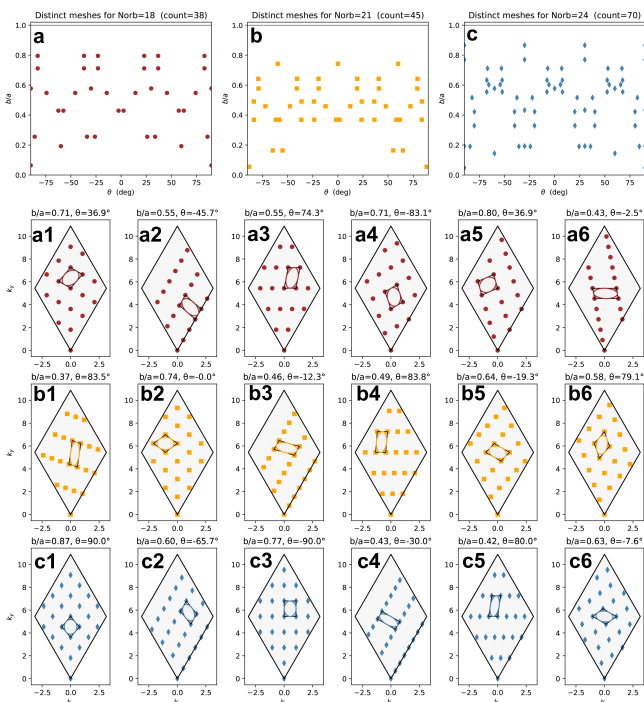


FIG. S5. (a, b, c) All Possible mesh at $N_{\text{orb}} = 18, 21, 24$. Each points represent a valid mesh. The "count" labels the total number of valid mesh. (ai, bi, ci with $i = 1, \dots, 6$) Examples of different kind of mesh for $N_{\text{orb}} = 18, 21, 24$.

variety of momentum-space meshes, each characterized by a unique parallelogram unit.

To quantify the anisotropic of each mesh, we inscribe an ellipse within its minimal parallelogram unit cell and define the eccentricity b/a of the ellipse as a proxy. A smaller b/a corresponds to a more elongated unit cell and hence stronger anisotropic character. Remarkably, we find that ED gaps decrease with b/a . The gap is defined as the energy difference between the fourth and third lowest many-body levels. Additionally, the orientation of the ellipse $\theta \in [0, \pi/3]$ (i.e., the angle between its major axis and the x -direction) also influences the FCI gap, though not in a strictly monotonic or causal way. Increasing the sampling density while holding eccentricity fixed (e.g., at $b/a = 0.71$) further enhances the stability of the FCI. Remarkably, when b/a is small nearly a thin torus [3], PES shows a cascade gap including CDW, $(1, 3)$ and $(1, 2)$ -counting rule [4], which can also be regraded as an indirect signature of unobserved $e/3$ -quasi-hole excitation origin from the vortex attachment of Halperin (112) typed ground states.

As illustrate in Fig. S5 (a-c), we calculate all possible mesh by scanning \tilde{M} matrix at fixed total number of orbitals N_{orb} . Each mesh is parameterized by $(b/a, \theta)$. Due to the intrinsic symmetry, the mesh only needs to take $\theta \in (0, 60^\circ]$. In the main text, ED calculation are carried on all these mesh to detect the intrinsic anisotropic influence. Different examples are also shown in S5 (a1-

a6, b1-b6, c1-c6).

B. Comparison of FCI-1 and conventional two components Halperin model states

Flat bands with ideal quantum geometry often support Halperin(mmn)-like FCIs with $m > n$. However, this is not the case in our system. Unlike standard Halperin-like FCIs, the FCI phase we observe exhibits a qualitatively different properties.

In the conventional construction of Abelian Halperin-like FCIs with $m > n$, the filling factor follows the relation $\nu = \frac{1}{m|C|+1}$, where m is odd for bosonic FCIs and even for fermionic FCIs [5]. Specifically, it is not possible to realize a fermionic FCI with threefold ground state degeneracy at $\nu = 1/3$ through this approach. The lowest possible case under this framework corresponds to a $\nu = 1/5$ (332)-like state, which features five folds degeneracy [6], in contradiction to our findings.

We also note that similar unconventional FCI states have been observed recently in other systems at $C = 2$, $\nu = 1/3$, and identified as Halperin (112) states, which exhibit the same PES counting as our results [7, 8]. The reasons is that Halperin (112) -state is the only two-components model phase support $C = 2/3$ with 3- folds degeneracy for a fermionic Abelian FCI. However, we argue that the counting of particle entanglement spectrum (PES) here is inconsistent with that of a conventional (112) states. For a PES match $(1, r)$ rule, we have the number of states below the PES gap satisfied,

$$D_{(1,r)}(N_{\text{orb}}, N_e) = \frac{N_{\text{orb}}}{N_e} \binom{N_{\text{orb}} - rN_e + N_e - 1}{N_e - 1}, \quad (\text{S51})$$

where $N_{\text{orb}} = N_x \times N_y$ and N_e is number of electrons [3]. While a standard Halperin (112) state should exhibit PES counting governed by the admissible- $(1, 3)$ rule, our system clearly follows the admissible- $(1, 2)$ rule, which similar to Laughlin- $1/2$ states with $e/2$ -excitations. This discrepancy can be traced back to the fact that the K-matrix of the (112) state can be transformed into that of the particle-hole conjugate of the Laughlin $\nu = 1/3$ state via an $SL(2, \mathbb{Z})$ transformation [9]. Therefore, the (112) state and the particle hole dual Laughlin $\nu = 1/3$ state should be regarded as belonging to the same topological order and have same PES [10]. We summary this argument in Tab. S1.

C. Admissible- $(1, 2)$ rule in FCI-1

At first glance, it seems impossible to generate an admissible $(1, 2)$ rule in an FCI whose elementary particles are electrons. However, we emphasize that this counting rule can be extracted not only from the ground states, but also from nearby excited states. As illustrated in

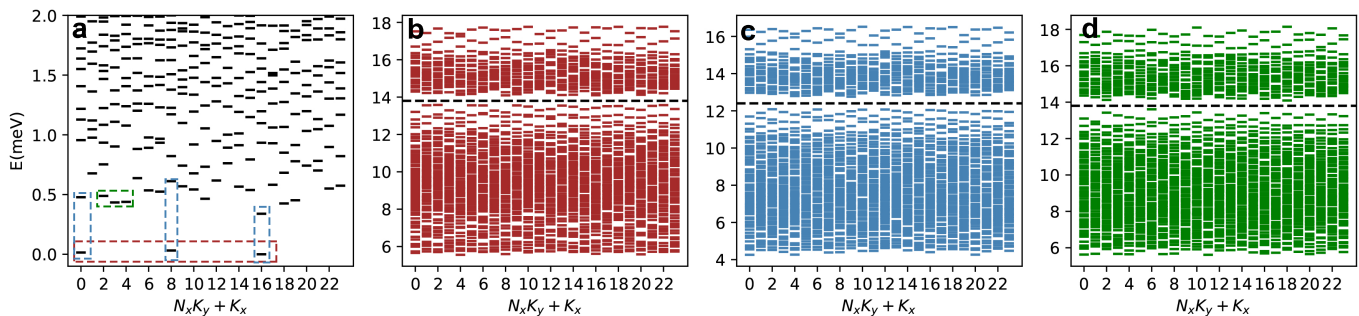


FIG. S6. (a) ED spectrum at $\kappa = 0.5$, the colored box indicate states that used to generated PES. (b-d) Corresponding PES extracted from different states labeled by colored box in (a), with $N_A = 3, N_B = 5$ and $D_{(1,2)}(24, 3) = 1520$ below the gap.

Fig. S6, considering only the ground states [Fig. S6(a,b)] yields the same PES as when excited states are included [Fig. S6(a,c)], and even when the ground states are entirely excluded [Fig. S6(a,d)]. This indicates that, in this case, the PES does not truly reflect the quasiparticle excitations of the ground state. The (1,2)-admissible counting, corresponding to $e/2$ quasiparticles, should be associated with higher-energy excitations, whereas the $e/3$ quasiholes that would normally be expected are no longer present.

D. Key numerical properties of FCI-1 at $\nu = 1/3$

. For $\kappa < 0.555$ at $\nu = 1/3$ filling, the system supports FCI that beyond the traditional Laughlin-like FCI. The key feature below,

1. As illustrate in Fig. S8 (a-c), when the mesh holds small eccentricity represent a thin tours i.e. $b/a = 0.19$, the PES spectrum supports cascade gaps at $N_A = 2$. The first gap indicate a charge density wave (CDW) phase, with the number of states below is $3C_{N_e=6}^{N_A}$, while the second gap indicate a standard admissible (1,3)-rules, grantee for Laughlin states. Meanwhile, the third gap appears satisfied the admissible (1,2)-rules which is non-trivial for it should indicate bosonic particle-hole excita-

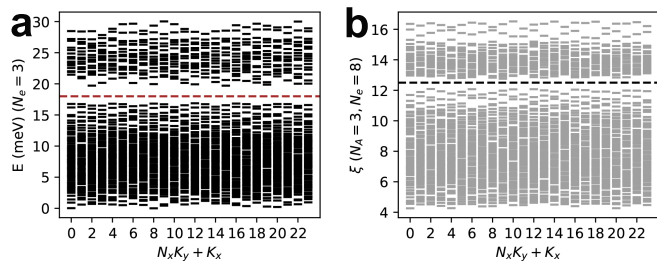


FIG. S7. (a) Comparison of ED results with $N_e = 3$ on 4×6 regular mesh. (b) PES results at $N_e = 8, N_A = 3$. All with 1520 states below the gap, satisfy admissible-(1,2) counting rule.

tions. We also consider the spectral function,

$$S(\mathbf{k}) = \frac{1}{N_{\text{orb}}} (\langle \rho(\mathbf{k}) \rho(-\mathbf{k}) \rangle - N_e^2 \delta_{\mathbf{k},0}) \quad (\text{S52})$$

where $\rho(\mathbf{k}) = \sum_{\mathbf{k}'} \hat{c}_{\mathbf{k}+\mathbf{k}'}^\dagger c_{\mathbf{k}'}$ is density operator. As illustrate in Fig. S8 (c), a peak appear at the K point of the Brillouin zone, consistent with CDW results.

2. As illustrate in Fig. S8 (d-f), when we increase $b/a = 0.41$, the CDW gap in PES disappear and the Laughlin-FCI PES gap also shrink. Compared with previous case, the ED gap also decrease. The remaining major gap shows admissible-(1,2) counting. Similarly, in this case, we compute $S(\mathbf{q})$, there is no pronounced peak anymore.

3. As illustrate in Fig. S8 (g-i), when we further make the mesh more isotropic with $b/a = 0.80$. we find both the CDW and (1,3)-counting gap closed in PES, with only (1,2)-gap remains. This results indicate the quasi-hole excitations are no-longer gaped with the particle-hole excitations. This can also being checked by performing ED calculation at $N_e = 2$ directly. As illustrate in Fig. S7, the ED results also gaped and show 153 states at lower energy sectors, providing a self-consistent prof of admissible (1,2)-counting rule.

E. Additional Exact Diagonalization results

As a supplement to the ED phase diagram presented in the main text, we provide additional exact diagonalization results at $\kappa = 0.5$, focusing on specific parameter cuts.

In Fig. S9(a), we show the evolution of the ground state as a function of interlayer potential bias, with all other parameters fixed. A robust FCI ground state is observed only within a narrow bias window between 40–60 meV. Outside this range, the system exhibits a unique ground state, which we identify as a conventional Fermi liquid (FL) phase.

In Fig. S9(b), we examine the role of the twist angle while keeping the remaining parameters identical to those used in the main text. The FCI-FL-gapless phase transitions are observed by tuning twist angle. The data

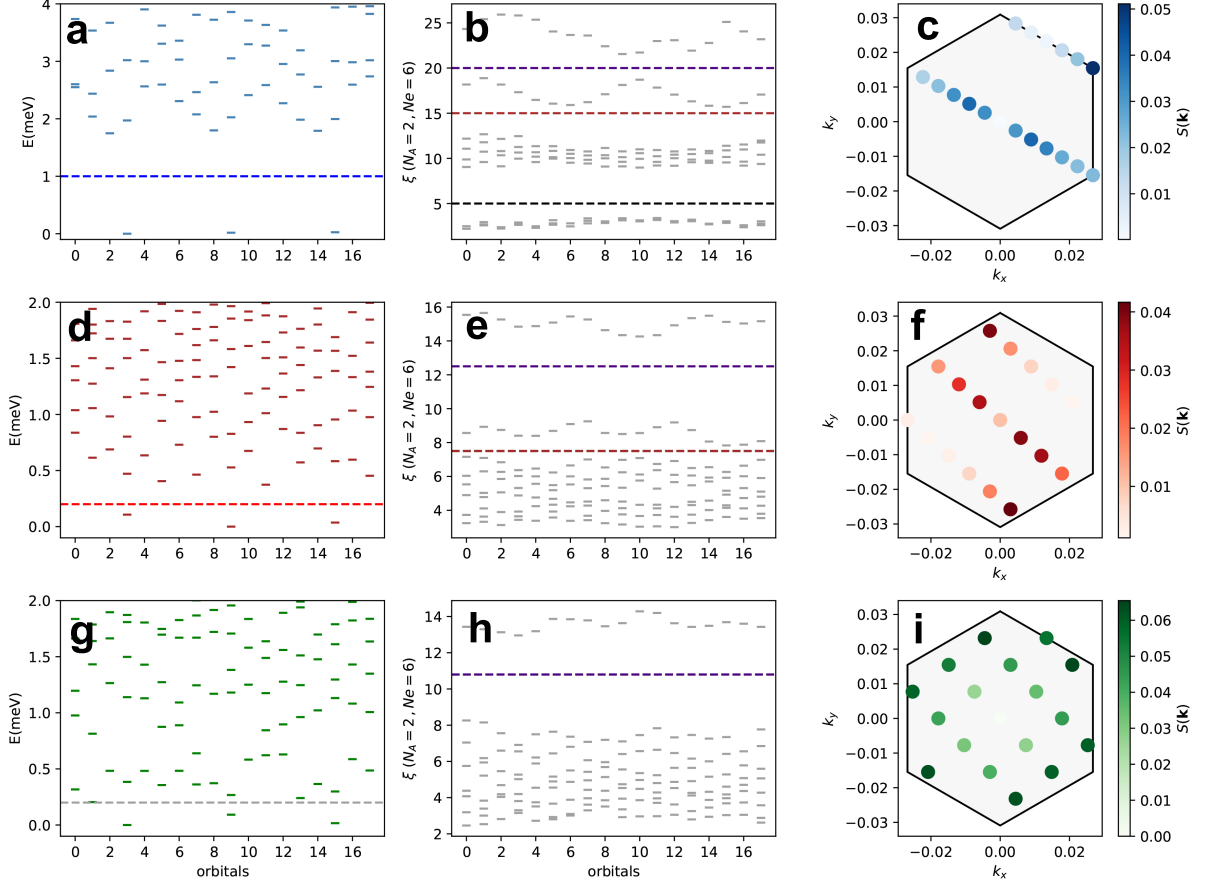


FIG. S8. (a-c) for $b/a = 0.19$ (d-f) for $b/a = 0.41$. (g-h) for $b/a = 0.71$ (a, d) 18-orbitals ED results with 3-fold degenerated ground states in $\nu = 1/3$. (b-e) PES with number of levels below black line is $3C_6^3 = 45$, red line is 117 as admissible-(1,3) rule and indigo line is 135 as (1,2) rule. (c,f,i) The spectral function to detect CDWs. (g) The ED results with 6 electrons on more isotropic mesh. (f) The PES with only 153 states below the gap, corresponding to the admissible-(1,2) rule.

FCI Type	Halperin (332)	Laughlin- $\bar{1}/3$ ^a	FCI-1 (Halperin (112)-like ground states) ^b
Hall Conductance σ_H	$2/5$	$2/3$	$2/3$
Ground-State Degeneracy	5	3	3
Quasiparticle Charge	$e/5$	$e/3$	$e/3$ ^c
PES (k, r) Counting	(1, 5)	(1, 3)	(1, 2) ^d
K -matrix of ground states	$\begin{pmatrix} 3 & 2 \\ 2 & 3 \end{pmatrix}$	$\begin{pmatrix} -3 & 0 \\ 0 & 1 \end{pmatrix}$	$\begin{pmatrix} 1 & 2 \\ 2 & 1 \end{pmatrix}$

^a Laughlin- $\bar{1}/3$ and Laughlin-1/3 are same topological order with same entanglement spectrum [11, 12]

^b Also $C = 2$ FCI in [7, 8], where PES show $D_{(1,2)}(3, 30) = 3250$ levels in both of their works.

^c Only observed through PES near thin torus see Fig. S8(b,e), but expected in general.

^d As illustrate in Fig. S6, not reflect quasiparticle excitation of standard Halperin-(112) ground states.

TABLE S1. Comparison of Fermionic FCI States.

reveal that the choice of twist angle $\theta = 1.04^\circ$, used in the main text, yields the clearest signature of an FCI: a well-isolated, nearly three-fold degenerate ground state.

Fig. S9(c) investigates the effect of the dielectric constant. Within the parameter regime used in the main text, we find no qualitative phase transition across the range $\epsilon = 3.0$ to 5.0. However, the quality of the three-

fold degeneracy degrades approximately linearly as the interaction strength weakens, indicating a gradual destabilization of the FCI.

Finally, in Fig. S9(d), we present the effect of inserting net flux through the system. The stability of the ground state under flux insertion further confirms the robustness of the FCI phase under the parameter choice employed

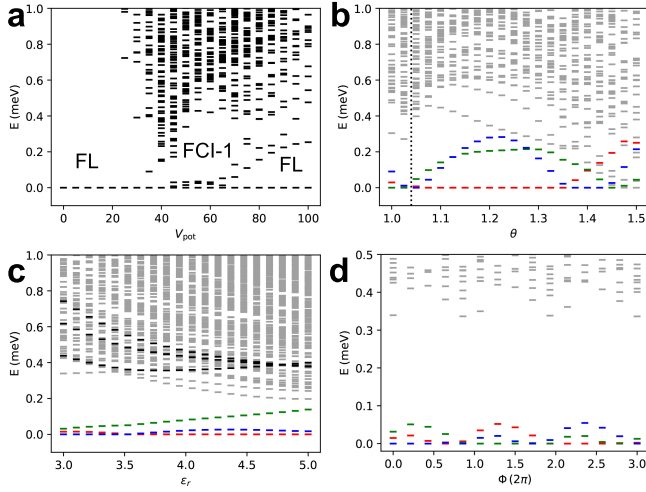


FIG. S9. The variation of ED spectrum (a) in terms of bias; (b) in terms of twist angle; (c) in terms of dielectric constant. (d) The special flow of Harperlin-like FCI.

in the main text.

F. Calculation details on Particle Entanglement Spectrum

To determine the topological phase of the ground states in our FCI system, we utilized the particle entanglement spectrum (PES) as a diagnostic tool, recognized for its ability to fingerprint topological order and indicate quasiparticle excitations. The ground states were expressed as $|\Omega_d\rangle = \sum_i e^{-\xi_i/2} |\Psi_i^A\rangle \otimes |\Psi_i^B\rangle$, where $e^{-\xi_i}$ and $|\Psi_i^A\rangle$ are the eigenvalues and eigenstates of the reduced density matrix $\rho_A = \text{Tr}_B(\rho)$, with the total density matrix defined by $\rho = \frac{1}{3} \sum_d |\Omega_d\rangle \langle \Omega_d|$.

The states $|\Psi_i^A\rangle$ were constructed block-diagonally within the bases $|l_A\rangle = \prod_{\mathbf{k} \in l_A} \eta_{\mathbf{k}}^\dagger |0\rangle$, representing configurations of N_A particles occupying orbital labels \mathbf{k} with total momentum $\mathbf{K}_A = \sum_{\mathbf{k} \in l_A} \mathbf{k}$. For each ground state sector with total momentum \mathbf{K}_d , the complementary momentum $\mathbf{K}_B = \mathbf{K}_d - \mathbf{K}_A$ defined the bases $|l_B\rangle$ for $N_B = N_e - N_A$ particles. In fermionic systems, the combined bases states were given by $|l\rangle = (-1)^{s_{AB}} |l_A\rangle \otimes |l_B\rangle$, where s_{AB} accounts for the fermionic sign from the ordering of orbital labels $\{k_1^A, \dots, k_{N_A}^A, k_1^B, \dots, k_{N_B}^B\}$, with each orbital label $k = N_x k_y + k_x$ enforcing the normal ordering $\eta_{k_1}^\dagger \dots \eta_{k_{N_e}}^\dagger \eta_{k_{N_e}} \dots \eta_{k_1}$ for $k_1 < k_2 < \dots < k_{N_e}$. The reduced density matrix elements were calculated as $[\rho_A]_{ij} = \sum_{l_B} (-1)^{(s_{A_i B} + s_{A_j B})} \Omega_{\{l_{A_i} \otimes l_B\}}^* \Omega_{\{l_{A_j} \otimes l_B\}}$, where $|\Omega\rangle = \sum_l \Omega_l |l\rangle$.

PES was computed independently across momentum sectors \mathbf{K}_A , with K_{Ax} ranging from 0 to N_x and K_{Ay} from 0 to N_y . The spectra were analyzed using $(k = 1, r = 2)$ -admissible partition rules, which restrict configurations to no more than one fermion per orbital and

no more than k fermions in $k + r$ consecutive orbitals. bases states $|l_v\rangle$ satisfying these criteria for N_A particles within an $N_x \times N_y$ orbital mesh were enumerated. A PES exhibiting an entanglement gap, where the number of entanglement energies below the gap matches the number of valid bases states $|l_v\rangle$, provided strong evidence of the ground states residing in the FCI phase.

G. Calculation of Many body Chern number

The mainly discussed FCI-1 $\kappa < 0.555$, $C = 2$ and FCI-2 $\kappa > 0.555$, $C = 1$ holds different many body Chern number consistent with previous HF results, thus the hall conductance also different. The many body Chern number is calculated with flux insertion $\mathbf{k} + \boldsymbol{\phi}$ where $\boldsymbol{\phi} = (\phi_x, \phi_y)$ and $\phi_\mu \in [0, 2\pi)$. The ground states can therefore be written as,

$$|\Omega_d(\boldsymbol{\phi})\rangle = \sum_l \Omega_{d,l}(\boldsymbol{\phi}) \prod_{\mathbf{k} \in l} \left(\sum_{\alpha, \mathbf{k}} u_{\mathbf{k}, \alpha}(\boldsymbol{\phi}) \hat{c}_{\mathbf{k}, \alpha}^\dagger |0\rangle \right), \quad (\text{S53})$$

where $d = 0, 1, 2$ is degenerated ground states label, $u_{\mathbf{k}, \alpha}(\boldsymbol{\phi}) = u_{k_x + \phi_x / (2\pi N_x), k_y + \phi_y / (2\pi N_y), \alpha}$ and $(k_x, k_y) \in (0 \dots N_x, 0 \dots N_y)$ is the single particle Hamiltonian eigenvectors of target flat bands, where $\alpha = (\mathbf{G}, \sigma, L)$ is composite index of reciprocal lattice, sublattices and layers. The core step in calculation is to evaluate the overlap of ground states at different flux insertion, using $\langle 0 | \hat{c}_{\mathbf{k}, \alpha}^\dagger \hat{c}_{\mathbf{k}', \beta} |0\rangle = \delta'_{\mathbf{k}, \mathbf{k}} \delta_{\alpha\beta}$ we have [13],

$$\begin{aligned} U_d(\boldsymbol{\phi}, \boldsymbol{\phi}') &:= \langle \Omega_d(\boldsymbol{\phi}) | \Omega_d(\boldsymbol{\phi}') \rangle \\ &= \sum_l \Omega_{d,l}^*(\boldsymbol{\phi}) \Omega_{d,l}(\boldsymbol{\phi}') \prod_{\mathbf{k} \in l} u_{\mathbf{k}, \alpha}^*(\boldsymbol{\phi}) u_{\mathbf{k}, \alpha}(\boldsymbol{\phi}') \end{aligned} \quad (\text{S54})$$

Therefore, the many body Chern number can be computed as,

$$C = \frac{1}{2\pi} \sum_d C_d = \sum_d \int_{\boldsymbol{\phi}} d\boldsymbol{\phi} F_d(\boldsymbol{\phi}) \quad (\text{S55})$$

with the berry curvature reads,

$$\begin{aligned} F_d(\boldsymbol{\phi}) &= U_d(\boldsymbol{\phi}, \boldsymbol{\phi} + d\boldsymbol{\phi}_x) U_d(\boldsymbol{\phi} + d\boldsymbol{\phi}_x, \boldsymbol{\phi} + d\boldsymbol{\phi}_x + d\boldsymbol{\phi}_y) \\ &\quad \times U_d(\boldsymbol{\phi} + d\boldsymbol{\phi}_x + d\boldsymbol{\phi}_y, \boldsymbol{\phi} + d\boldsymbol{\phi}_y) U_d(\boldsymbol{\phi} + d\boldsymbol{\phi}_y, \boldsymbol{\phi}) \end{aligned} \quad (\text{S56})$$

where $d\phi_\mu = 2\pi/N_{\phi_\mu}$. Here, we take $N_{\phi_x} \times N_{\phi_y} = 10 \times 10$. As illustrate in Fig. S10, the resulting fractional Chern number $C_d \approx 2/3$ for each momentum sector at $\kappa = 0.5$ are $C_1 = 0.62223074$, $C_2 = 0.69359348$, $C_3 = 0.68729438$ with total Chern number $C = 2.003$ and $C_d \approx 1/3$ with $C_1 = 0.35996735$, $C_2 = 0.34924193$, $C_3 = 0.29389492$ and total Chern number $C = 1.003$ for $\kappa = 0.7$.

H. Fidelity diagnostic

To diagnose the quantum phase transition we compute the fidelity between ground states at neighboring values

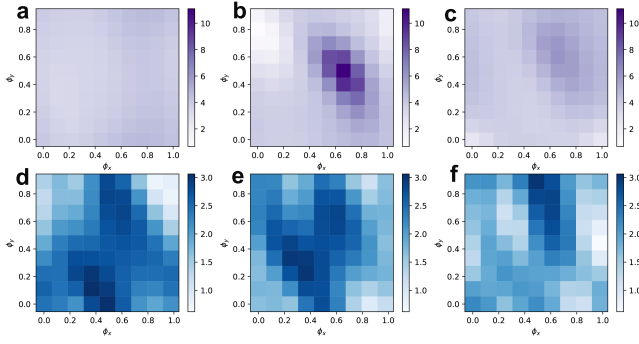


FIG. S10. (a-c) The berry curvature for FCI-1 at $\kappa = 0.5$ in terms of three ground states, the resulting $C_d \approx 2/3$ for each figure is not standard Lauglin-like. (d-f) Same results for FCI-2 in $\kappa = 0.7$ with $C_d \approx 1/3$, which is a standard Lauglin-like results.

of the tuning parameter κ . For each κ we diagonalize the many-body Hamiltonian in fixed total-momentum sectors K , and denote by

$$|\Psi_K(\kappa)\rangle = \sum_{\{n\}} C_K(\{n\}; \kappa) |\{n\}\rangle \quad (\text{S57})$$

the lowest-energy state in sector K , expanded in the occupation-number basis $\{|\{n\}\rangle\}$ of the ED Hilbert space. In our problem the topological ground state is three-fold degenerate, with one state in each of the momentum sectors $K \in K_D$ (typically $|K_D| = 3$).

Because of this exact (or near) degeneracy the individual vectors $|\Psi_K(\kappa)\rangle$ are only defined up to a κ -dependent $U(|K_D|)$ rotation within the ground-state manifold. To obtain a gauge-invariant quantity we work with the equal-weight mixed density matrix

$$\rho(\kappa) = \frac{1}{N_{\text{GS}}} \sum_{K \in K_D} |\Psi_K(\kappa)\rangle \langle \Psi_K(\kappa)|, \quad N_{\text{GS}} = |K_D|. \quad (\text{S58})$$

$$\langle \Psi_K(\kappa) \Psi_K(\kappa + \delta\kappa) \rangle = \sum_{\{n\}} C_K^*(\{n\}; \kappa) S_{\{n\}}(\kappa) C_K(\{n\}; \kappa + \delta\kappa). \quad (\text{S63})$$

Finally, these sector-resolved overlaps are combined according to Eq. (S60) to produce the density-matrix fidelity $F(\kappa, \kappa + \delta\kappa)$ used in the main text.

I. Details on Particle Entanglement Spectrum transition

Here, we present detailed results on the evolution of the particle entanglement spectrum (PES) in Fig. S11. Specifically, for κ ranging from 0 to approximately 0.55,

The fidelity between two nearby points κ and $\kappa + \delta\kappa$ is defined as the Uhlmann fidelity between the corresponding density matrices,

$$F(\kappa, \kappa + \delta\kappa) = \left[\text{Tr} \sqrt{\sqrt{\rho(\kappa)} \rho(\kappa + \delta\kappa) \sqrt{\rho(\kappa)}} \right]^2. \quad (\text{S59})$$

In our case states belonging to different total-momentum sectors are orthogonal, so $\rho(\kappa)$ is a direct sum of rank-one projectors. Equation (S59) then simplifies to

$$F(\kappa, \kappa + \delta\kappa) = \frac{1}{N_{\text{GS}}^2} \left(\sum_{K \in K_D} |\langle \Psi_K(\kappa) | \Psi_K(\kappa + \delta\kappa) \rangle|^2 \right), \quad (\text{S60})$$

so that the only input needed is the overlap between the many-body ground states in the same momentum sector.

These overlaps are evaluated efficiently by expressing the ground states in terms of the κ -dependent single-particle eigenvectors. Denoting by $u_{ka}(\kappa)$ the single-particle Bloch eigenvectors (labelled by orbital index k and band index a), we first compute the diagonal single-particle overlaps

$$s_k(\kappa) = \sum_a u_{ka}^*(\kappa) u_{ka}(\kappa + \delta\kappa). \quad (\text{S61})$$

For a many-body basis state $|\{n\}\rangle = \prod_k (c_k^\dagger)^{n_k} |0\rangle$ with occupations $n_k \in \{0, 1\}$, the corresponding diagonal overlap factor is

$$S_{\{n\}}(\kappa) = \prod_{k | n_k=1} s_k(\kappa). \quad (\text{S62})$$

Inserting this into the expansion of $|\Psi_K(\kappa)\rangle$ and $|\Psi_K(\kappa + \delta\kappa)\rangle$ in the occupation basis, we obtain

we observe a well-defined entanglement gap near $\xi \approx 13.8$, below which there are exactly 1520 states. This counting is consistent with the (1,2)-generalized Pauli exclusion principle, which is not typical-Lauglin type in $\nu = 1/3$ for fermions. As κ increases, the trace condition deteriorates further, suggesting the eventual breakdown of the FCI phase. However, intriguingly, the PES shows the emergence of entanglement gap around $\xi \approx 11$. Below this gap, there are exactly 1088 levels, matching the generalized Pauli principle where no more than one particle occupies any triplet of consecutive orbitals. This

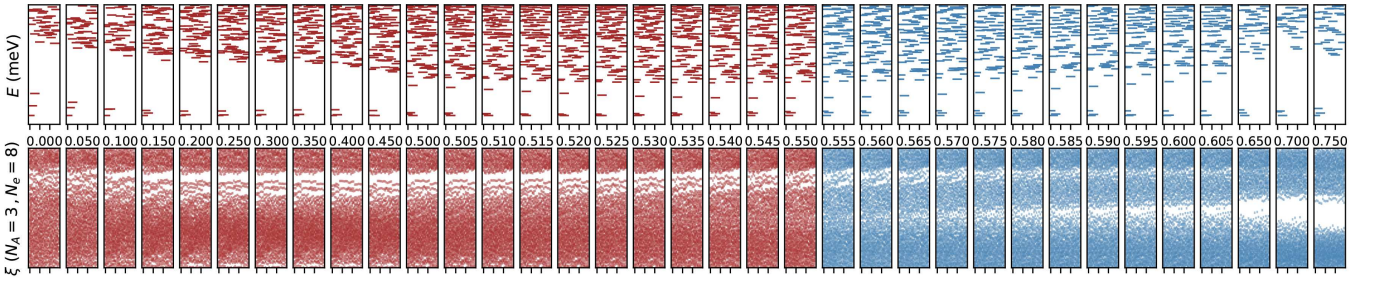


FIG. S11. Details on ED (Upper) and PES (lower) transition in the main text Fig. 2, where x-axis is total momentum label $K_x + N_x K_y$ with $(N_x, N_y) = (4 \times 6)$. The number between two rows are $\kappa \in [0, 0.75]$. Red and blue colors represent FCI-1 and FCI-2.

level counting aligns precisely with that expected from a Laughlin-type state, indicating a transition in the underlying exclusion statistics.

S4. LANDAU LEVEL EXPANSION UNDER MAGNETIC FIELD

In the presence of a perpendicular magnetic field, the band structure of tMBG develops Landau quantization and fractal minibands characteristic of the Hofstadter spectrum. To describe this, we define the guiding center coordinate along y as

$$Y_{M,j} = k_x l^2 + (Mp + j)\Delta, \quad (\text{S64})$$

where $l = \sqrt{\hbar/eB}$ is the magnetic length, p and q are integers specifying the magnetic flux per moiré unit cell $\Phi/\Phi_0 = p/6q$, and $\Delta = Q_x l^2$ is the y -direction spacing between adjacent guiding centers [14].

The intralayer Hamiltonian in the Landau level basis reads

$$h_\theta^\pm = -\hbar\omega_c e^{\pm i\theta/2} \begin{bmatrix} 0 & \delta_{n+1,n} \\ \delta_{n,n+1} & 0 \end{bmatrix} \otimes \sum_Y |YL\rangle\langle YL|, \quad (\text{S65})$$

with $\omega_c = \sqrt{2}v_0/l$ the cyclotron frequency, and n the Landau level index.

The AB-stacked interlayer coupling becomes

$$G = \begin{bmatrix} -\hbar v_4 \sqrt{2}/l \delta_{n,n+1} e^{-i\theta/2} & \gamma_1 \\ -\hbar v_3 \sqrt{2}/l \delta_{n+1,n} e^{-i\theta/2} & -\hbar v_4 \sqrt{2}/l \delta_{n,n+1} e^{-i\theta/2} \end{bmatrix} \otimes \sum_Y |Y2\rangle\langle Y1| + \text{h.c.}, \quad (\text{S66})$$

where $|Y1\rangle$, $|Y2\rangle$ denote states on the first and second layers.

The moiré interlayer coupling becomes momentum dependent and takes the form

$$T(k_x, k_y) = \sum_{m,n,\alpha,\beta,j} \sum_{s=1}^3 T_j^{(s)} |2m\alpha j\rangle \langle 1n\beta j|, \quad (\text{S67})$$

with $T_j^{(s)}$ the tunneling matrices associated with momentum transfer \mathbf{q}_s , and matrix elements given by

$$T_j^{(1)} = T_1 F_{mn}(z_1) e^{-ik_\theta y_0} e^{-4\pi i j q/p}, \quad (\text{S68})$$

$$T_j^{(2)} = T_2 F_{mn}(z_2) e^{ik_y \Delta} e^{ik_\theta y_0} e^{i\pi(2j-1)q/p}, \quad (\text{S69})$$

$$T_j^{(3)} = T_3 F_{mn}(z_3) e^{-ik_y \Delta} e^{ik_\theta y_0} e^{i\pi(2j+1)q/p}, \quad (\text{S70})$$

where $y_0 = k_x l^2$ and $z_s = \frac{l}{\sqrt{2}}(q_{s,x} + iq_{s,y})$. The function $F_{mn}(z)$ is the generalized Landau level form factor

$$F_{mn}(z) = \langle m | e^{z^* \hat{a}^\dagger - z \hat{a}} | n \rangle, \quad (\text{S71})$$

with closed-form expressions involving associated Laguerre polynomials:

$$F_{mn}(z) = \begin{cases} \sqrt{\frac{n!}{m!}} (z^*)^{m-n} L_n^{(m-n)}(|z|^2) e^{-\frac{|z|^2}{2}}, & m \geq n, \\ \sqrt{\frac{m!}{n!}} (-z)^{n-m} L_m^{(n-m)}(|z|^2) e^{-\frac{|z|^2}{2}}, & n > m. \end{cases} \quad (\text{S72})$$

The full Hamiltonian has dimension $6Np$, where N is the number of Landau levels kept, and $6 = 2$ (sublattices) $\times 3$ (layers). For the $-K$ valley, one can obtain the corresponding Hamiltonian by flipping the signs of magnetic flux.

A. Quantum geometry under magnetic field

At finite magnetic field the computation of band geometry differs in two essential ways from the zero-field case. First, the presence of magnetic translations implies that Bloch's theorem holds only in a magnetic Brillouin zone (MBZ) defined at rational flux $\phi = p/q$, with twisted boundary conditions for the periodic part of the wavefunction. Concretely, the commuting set of magnetic translations emerges only after enlarging the real-space unit cell by a factor of q , and eigenstates $|\psi_{\mathbf{a}\mathbf{k}}\rangle$ then obey $M(\mathbf{R})|\psi_{\mathbf{a}\mathbf{k}}\rangle = e^{i\mathbf{k}\cdot\mathbf{R}}|\psi_{\mathbf{a}\mathbf{k}}\rangle$ with \mathbf{k} restricted to the MBZ (there are q times as many bands at each \mathbf{k}). This MBZ folding and the associated twisted phases must be respected when discretizing k -space for geometry. :contentReference[oaicite:0]index=0

Second—and crucial for practical evaluation—the use of a Landau-level basis injects *intrinsic curvature* from the basis itself, so the standard zero-field overlap formulas cannot be used naively. As shown in the supplemental derivation, the Landau-level basis carries an analytic, band-diagonal Berry-curvature contribution; hence both the Berry curvature and the quantum geometric tensor (QGT) require a modified, gauge-covariant construction. In the single-band (U(1)) limit this appears as an explicit correction $F = F_{\text{numerical}} - 1/p$, but for the general multi-band (U(N)) case the answer is not a simple “numerical plus analytic” sum and must be extracted from a Wilson-loop formulation [15].

A numerically stable and gauge-invariant route is to compute the non-Abelian Berry curvature from the holonomy of a minimal Wilson loop on the k -mesh, $e^{iF(\mathbf{k})\Delta k_x\Delta k_y} = W_{\square}(\mathbf{k}) = U_{\mathbf{k},\mathbf{k}+\Delta_x} U_{\mathbf{k}+\Delta_x,\mathbf{k}+\Delta_x+\Delta_y} U_{\mathbf{k}+\Delta_x+\Delta_y,\mathbf{k}+\Delta_y} U_{\mathbf{k}+\Delta_y,\mathbf{k}}$, with link matrices $[U_{\mathbf{k},\mathbf{k}'}]_{ab} = \langle U_a(\mathbf{k})|U_b(\mathbf{k}') \rangle$ built from

$$W_{\square} = e^{-i\frac{2\pi}{N_x N_y p}} (V_x)_{\mathbf{k},\mathbf{k}+\Delta_x} (V_y)_{\mathbf{k}+\Delta_x,\mathbf{k}+\Delta_x+\Delta_y} (V_x^\dagger)_{\mathbf{k}+\Delta_x+\Delta_y,\mathbf{k}+\Delta_y} (V_y^\dagger)_{\mathbf{k}+\Delta_y,\mathbf{k}}, \quad (\text{S73})$$

with $(V_\alpha)_{\mathbf{k},\mathbf{k}'} = \sum_{I,J} \psi_a^I(\mathbf{k}) T_\alpha^{IJ} \psi_b^J(\mathbf{k}')$ and T_α the analytic LL transport matrices on the corresponding link [15]. This expression implements the necessary subtraction/compensation of the LL-basis curvature in a gauge-covariant way and provides a robust numerical formula for the Berry curvature (from the eigenphases of W_{\square}) on the MBZ. The quantum metric under field is obtained analogously by evaluating suitable “back-and-forth” Wilson paths (e.g. $k \rightarrow k + q_\alpha e_\alpha \rightarrow k$) with the same LL analytic factors included on each link; in this way both curvature and metric are computed consistently from the same non-Abelian transport that cleanly separates the LL contribution from the numerically determined band mixing.

Finally, we note practical considerations specific to the LL expansion: the single-particle Hamiltonian at fixed \mathbf{k} is countably infinite-dimensional in the LL index and must be truncated at $n, m < N$; the resulting matrix elements inherit Laguerre-form-factor structure that decays rapidly with $|m-n|$, ensuring numerical tractability while preserving the analytic LL transport used above. These implementation details are orthogonal to the geometry formulas but crucial for stable evaluation of W_{\square} in large- q MBZs.

B. Landau fan of Wannier plot

We construct a Wannier-style Landau fan by scanning rational fluxes $\phi = p/q$ and, at each ϕ , computing the single-particle spectrum $\{\varepsilon_n(\mathbf{k}; \phi)\}$ over the MBZ (or equivalently over magnetic Bloch momenta). either re-

an orthonormal frame $\{|U_a(\mathbf{k})\rangle\}$ spanning the target band subspace. In a Landau-level implementation the eigenstates are expanded as $|U_a(\mathbf{k})\rangle = \sum_I \psi_a^I(\mathbf{k}) |u_I(\mathbf{k})\rangle$ where I collects internal labels (layer/sublattice/spin), the Landau-level index n , and the guiding-center index j . The corresponding link overlaps factor into a *numerical* part from the coefficients ψ_a^I and an *analytic* part from the Landau-level transport, so that one must separate the LL analytic parallel transport on each link before forming the plaquette [15].

Operationally, this factorization appears explicitly in the x/y -link matrices. In Landau gauge, the y -link carries an extra exponential phase that is precisely the band-diagonal LL correction; upon taking the plaquette and tracing the holonomy, this yields a net shift of $(2\pi)^{-1} \int \text{tr} F$ by $1/p$ per band in the U(1) limit. The full non-Abelian Wilson operator for a plaquette on an $N_x \times N_y$ mesh at flux p/q can be written

solved or combined as appropriate. To visualize gaps uniformly across different ϕ we replace discrete levels with a Lorentzian-broadened density of states (DOS),

$$\rho(E; \phi) = \frac{1}{N_k} \sum_{n,\mathbf{k}} \frac{1}{\pi} \frac{\Gamma(\phi)}{[E - \varepsilon_n(\mathbf{k}; \phi)]^2 + \Gamma(\phi)^2}, \quad (\text{S74})$$

where N_k is the MBZ k -mesh size. The broadening $\Gamma(\phi)$ is a plotting parameter chosen to balance visibility and gap resolution; one may take a constant Γ_{vis} for all ϕ or an adaptive choice such as $\Gamma(\phi) = \alpha$ times a representative bandwidth at that flux. For a chosen chemical potential (energy cutoff) μ we define the filling (per magnetic unit cell and per internal flavor, unless otherwise stated) by

$$n(\mu, \phi) = \int_{-\infty}^{\mu} \rho(E; \phi) dE. \quad (\text{S75})$$

As illustrate in Fig. S12, we then plot n versus $\phi = p/q$ and color the points by $\rho(\mu; \phi)$ (or, equivalently, mark local minima of the DOS). Along spectral gaps the DOS is minimal and the graph $n(\phi)$ aligns into nearly straight “gap lines.” These lines obey the Diophantine/St eda relation

$$n(\mu, \phi) = t\phi + \nu, \quad \phi = \frac{p}{q}, \quad (\text{S76})$$

with an integer intercept ν and an integer slope t that equals the Chern-number difference across the gap; for a gap above a set of fully occupied bands, t equals the total Chern number of those occupied bands. Operationally,

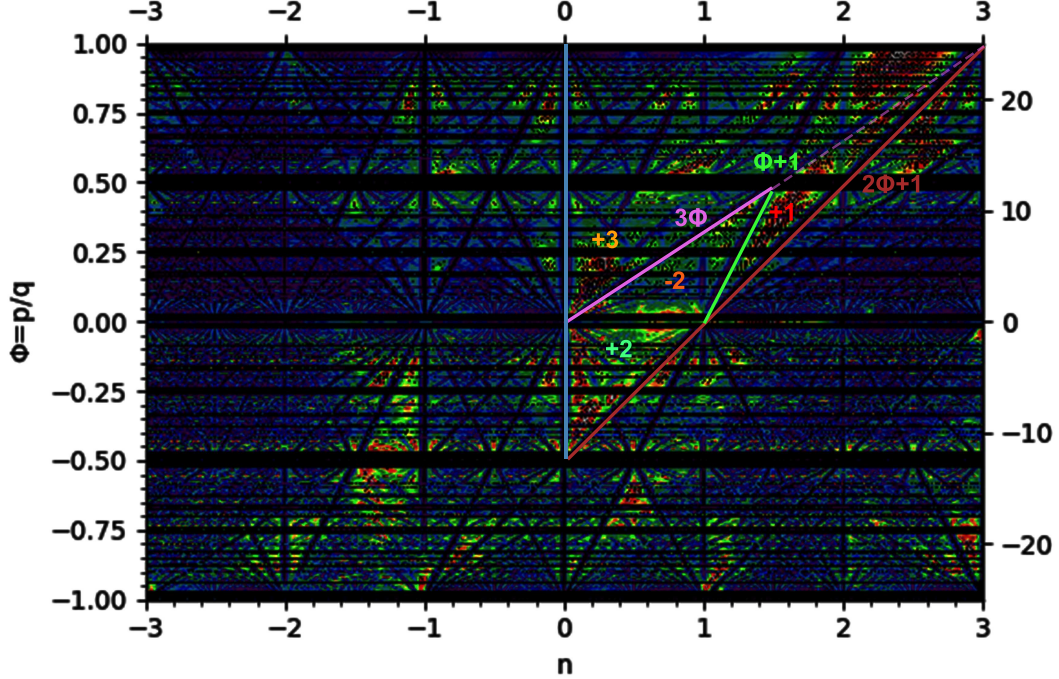


FIG. S12. The Wannier plot of Hofstadter butterfly spectrum. The colored line gives $n = C\Phi + \nu$ represent Diophantine equations of gaps. The Chern number of states are also labeled. The highlighted area is mainly considered region in the main text.

one collects the (ϕ, n) points where ρ is locally minimal for a given gap and performs a linear fit to extract (t, ν) ; repeating this across gaps produces the Landau fan of straight rays with integer slopes. Finally, as a non-visual check, we compute Chern numbers independently from

Berry curvature (e.g., by Wilson loops on the same MBZ mesh) and confirm that the slopes t obtained from the fan coincide with the corresponding topological invariants. This procedure yields a gap-by-gap topological labeling from the DOS alone, and, by construction, agrees with the Berry-curvature integral results.

-
- [1] Y. H. Kwan, J. Yu, J. Herzog-Arbeitman, D. K. Efetov, N. Regnault, and B. A. Bernevig, [Moiré fractional chern insulators iii: Hartree-fock phase diagram, magic angle regime for chern insulator states, the role of the moiré potential and goldstone gaps in rhombohedral graphene superlattices](#) (2023), [arXiv:2312.11617 \[cond-mat.str-el\]](#).
- [2] J. Yu, J. Herzog-Arbeitman, Y. H. Kwan, N. Regnault, and B. A. Bernevig, [Moiré fractional chern insulators iv: Fluctuation-driven collapse of fcis in multi-band exact diagonalization calculations on rhombohedral graphene](#) (2024), [arXiv:2407.13770 \[cond-mat.str-el\]](#).
- [3] B. A. Bernevig and N. Regnault, [Thin-torus limit of fractional topological insulators](#) (2012), [arXiv:1204.5682 \[cond-mat.str-el\]](#).
- [4] See supplemental material, [URL will be inserted by publisher], for details on HF, ED and magnetic model calculations.
- [5] Z. Liu and E. J. Bergholtz, Recent developments in fractional chern insulators, in [Encyclopedia of Condensed Matter Physics](#) (Elsevier, 2024) p. 515–538.
- [6] J. Dong, P. J. Ledwith, E. Khalaf, J. Y. Lee, and A. Vishwanath, Many-body ground states from decomposition of ideal higher chern bands: Applications to chirally twisted graphene multilayers, [Phys. Rev. Res.](#) **5**, 023166 (2023).
- [7] Y. Liu and Z. Zhu, Engineering fractional chern insulators through periodic strain in monolayer graphene and transition metal dichalcogenides, [Phys. Rev. B](#) **112**, L041123 (2025).
- [8] S. Niu, J. Alicea, D. N. Sheng, and Y. Peng, Quantum anomalous hall effects and emergent $su(2)$ hall ferromagnets at fractional filling of helical trilayer graphene, [Phys. Rev. Lett.](#) **135**, 146505 (2025).
- [9] X.-G. Wen, [Quantum Field Theory of Many-Body Systems: From the Origin of Sound to an Origin of Light and Electrons](#) (Oxford University Press, Oxford, 2004).
- [10] S. Geraedts, M. P. Zaletel, Z. Papić, and R. S. K. Mong, Competing abelian and non-abelian topological orders in $\nu = 1/3 + 1/3$ quantum hall bilayers, [Phys. Rev. B](#) **91**, 205139 (2015).
- [11] A. Sterdyniak, A. Chandran, N. Regnault, B. A. Bernevig, and P. Bonderson, Real-space entanglement

- spectrum of quantum hall states, *Phys. Rev. B* **85**, 125308 (2012).
- [12] L. Hu and W. Zhu, Abelian origin of $\nu = 2/3$ and $2+2/3$ fractional quantum hall effect, *Phys. Rev. B* **105**, 165145 (2022).
- [13] S. Okamoto, N. Mohanta, E. Dagotto, and D. N. Sheng, Topological flat bands in a kagome lattice multiorbital system, *Commun. Phys.* **5**, 198 (2022).
- [14] R. Bistritzer and A. H. MacDonald, Moiré butterflies in twisted bilayer graphene, *Phys. Rev. B* **84**, 035440 (2011).
- [15] Y. L. Xie, A. T. Pierce, J. M. Park, D. E. Parker, E. Khalaf, P. Ledwith, Y. Cao, S. H. Lee, S. W. Chen, P. R. Forrester, K. Watanabe, T. Taniguchi, A. Vishwanath, P. Jarillo-Herrero, and A. Yacoby, Fractional chern insulators in magic-angle twisted bilayer graphene, *Nature* **600**, 439 (2021).